Homogenized lattice Boltzmann model for simulating multi-phase flows in heterogeneous porous media

Martin P. Lautenschlaeger [a,b,*], Julius Weinmiller [a,b], Benjamin Kellers [a,b], Timo Danner [a,b], Arnulf Latz [a,b,c]

[a] *German Aerospace Center (DLR), Institute of Engineering Thermodynamics, 70569 Stuttgart, Germany*
[b] *Helmholtz Institute Ulm for Electrochemical Energy Storage (HIU), 89081 Ulm, Germany*
[c] *Ulm University (UUlm), Institute of Electrochemistry, 89081 Ulm, Germany*

ARTICLE INFO

ABSTRACT

A homogenization approach for the simulation of multi-phase flows in heterogeneous porous media is presented. It is based on the lattice Boltzmann method and combines the grayscale with the multi-component Shan–Chen method. Thus, it mimics fluid–fluid and solid–fluid interactions also within pores that are smaller than the numerical discretization. The model is successfully tested for a broad variety of single- and two-phase flow problems. Additionally, its application to multi-scale and multi-phase flow problems in porous media is demonstrated using the electrolyte filling process of realistic 3D lithium-ion battery electrode microstructures as an example. The approach presented here shows advantages over comparable methods from literature. The interfacial tension and wetting conditions are independent and not affected by the homogenization. Moreover, all physical properties studied here are continuous even across interfaces of porous media. The method is consistent with the original multi-component Shan–Chen method (MCSC). It is as stable as the MCSC, easy to implement, and can be applied to many research fields, especially where multi-phase fluid flow occurs in heterogeneous and multi-scale porous media.

1. Introduction

Fluid flow in porous media plays an important role in many technical and natural processes such as hydrogeology, reservoir and process engineering, electrochemical energy storage, or medical applications. Most of these examples involve complex flow phenomena such as transport of solutes, reactions, or the interaction of multiple phases or immiscible fluid components (Kang et al., 2007; Dentz et al., 2011; Steefel et al., 2005; Baveye et al., 2017; Laubach et al., 2019; Yuan et al., 2019), structures that are heterogeneous regarding their chemical composition and wetting properties (Dentz et al., 2011; Blunt et al., 2013; Laubach et al., 2019; Zhang et al., 2020), and pore sizes that range from nanometers to the macroscale (Sok et al., 2010; Bai et al., 2013; Blunt et al., 2013; Zhang et al., 2016; Kang et al., 2019; Soulaine et al., 2019; Zhang et al., 2020; Mehmani et al., 2020). Thus, and because most of the interesting physical phenomena happen on the pore scale, they are hard to study experimentally (Sok et al., 2010; Kang et al., 2002b; Dentz et al., 2011; Mehmani et al., 2020).

Therefore, in the literature often direct numerical simulations and more specifically the lattice Boltzmann method (LBM) are used to conduct pore-scale simulations. LBM is a reliable tool for studying multi-scale and multi-physics transport processes within complex porous

geometries (Krueger et al., 2016; Liu et al., 2016). It has also been successfully applied to solve multi-phase flows in high-resolution real-world image data of porous media samples that were recorded using X-ray micro-computed tomography (μ-CT) or focused ion beam scanning electron microscopy (FIB-SEM) (Sok et al., 2010; Blunt et al., 2013; Chen et al., 2014; Liu et al., 2016; Zhang et al., 2016; Baveye et al., 2017; Kang et al., 2019; Zhang et al., 2020; Mehmani et al., 2020).

Unfortunately, LBM is computationally expensive, especially when simultaneously simulating flow in structurally resolved pores at different length scales. Therefore, homogenization methods have been developed, where the detailed structure of pores at the smallest length scale is ignored and, instead, the flow is described by a Darcy–Brinkman-type approach. A volume average of the structurally resolved geometry is taken and its effects on fluid flow are mimicked as permeability-related parameter. These homogenization methods can be basically subdivided into two groups. Those are the Brinkman force-adjusted models (BF) (Spaid and Phelan, 1997; Freed, 1998; Guo and Zhao, 2002; Kang et al., 2002b; Ginzburg, 2008; Gao et al., 2014; Ginzburg et al., 2015; Kang et al., 2019), where a drag force is applied locally, and the grayscale models (GS) (Dardis and McCloskey, 1998; Thorne

---

and Sukop, 2004; Chen and Zhu, 2008; Walsh et al., 2009; Zhu and Ma, 2013; Yoshida and Hayashi, 2014; Yehya et al., 2015; Ginzburg et al., 2015; Ginzburg, 2016; Zhu and Ma, 2018), where flow populations are partially bounced back to mimic flow resistance.

Although the aforementioned homogenization methods have been heavily discussed and further developed for single-phase fluids (Chen and Zhu, 2008; Walsh et al., 2009; Zhu and Ma, 2013; Ginzburg et al., 2015; Ginzburg, 2016; Zhu and Ma, 2018), this is not the case for multi-phase or multi-component fluids. Only a few methods combining GS and multi-phase physics (McDonald and Turner, 2016; Zalzale et al., 2016; Lei and Shi, 2019) as well as methods combining other homogenization approaches with multi-component physics (Ning et al., 2019; An et al., 2020) have been reported recently. However, despite the fact that the multi-component Shan–Chen method (MCSC) is most widely used for studying all kinds of immiscible fluids (Chen et al., 2014; Krueger et al., 2016), only one homogenized method has been developed combining GS with MCSC (Pereira, 2016). This method is however not fully consistent with the original MCSC regarding model parametrization and shows deficiencies with respect to discontinuities of properties in heterogeneous porous media.

Therefore, in the current paper, a new approach is presented, that follows the approach of Pereira (2016) and combines GS by Walsh et al. (GS-WBS) (Walsh et al., 2009) with MCSC (Shan and Chen, 1993). It is therefore called the homogenized multi-component Shan–Chen method (HMCSC) in the following. GS-WBS is chosen as it is known to recover Darcy–Brinkman flow, conserves mass, and allows an efficient computational parallelization as only local bounce-back operations are performed. MCSC uses a physically-based approach to model fluid–fluid and solid–fluid interactions without the need for interface tracking. It also achieves a good compromise between computational efficiency and physical reality, and thus is widely adopted for modeling immiscible fluids (Chen et al., 2014; Krueger et al., 2016).

The HMCSC inherits all positive features from the aforementioned models, but overcomes their deficiencies which are mainly related to the discontinuity of properties in heterogeneous porous media. For example, using HMCSC, the interfacial tension and the wetting properties are constant and not affected by the homogenization. Thus, especially the MCSC-related model parameters can be chosen consistently to the original MCSC and no further parametrization is required. Besides, similar to all other LBM homogenization approaches, the HMCSC switches freely between free-flow and Darcy regime, and can also be applied to study single-phase flows.

As part of this paper, the HMCSC was rigorously tested for a broad variety of single-phase and two-phase flow benchmark cases that are relevant in the context of porous media. Those were Stokes–Brinkman–Darcy flow under Couette and Poiseuille conditions, fluid flow in stratified heterogeneous porous media and partially porous channels, as well as steady bubble tests and Washburn-type capillary flow. It was also tested regarding its numerical stability and shown to be comparable to the original MCSC. In addition, it predicts Buckley–Leverett waterflooding to some extent (cf. Section SI-3 in the Supporting Information). The results were compared with analytical and semi-analytical solutions where available. Finally, the HMCSC was applied to a two-phase flow issue of current research interest in the field of electrochemical energy storage: The electrolyte filling of lithium-ion battery microstructures with partially permeable nanoporous components. However, other research fields where multi-phase fluid flow occurs in multi-scale porous media can benefit from the new method, too. In the context of hydrology, geoscience and petroleum engineering, potential applications are the prediction of microbiologically affected groundwater flow (Ghezzehei, 2012; Hassannayebi et al., 2021), geologic carbon storage or sequestration (Krevor et al., 2012; Mehmani and Tchelepi, 2018), and the recovery of oil, dry natural gas, or shale gas from tight gas sandstones (Mehmani et al., 2015, 2020), carbonates (Mehmani et al., 2015, 2020) and shale formations (Soulaine et al., 2019), respectively.

This paper is organized as follows. In Section 2, the HMCSC is described. In Section 3, it is tested for a broad variety of benchmark cases and the corresponding results, features of the approach, and its numerical stability are discussed. In Section 4, the results of the electrolyte filling simulations in realistic and partially homogenized battery microstructures are presented. Finally, conclusions are drawn in Section 5.

2. Model

The LBM fundamentals, including the determination of macroscopic variables, as well as the underlying methods are given in Appendix A. For further information, especially regarding GS-WBS and MCSC, the reader is directed to the corresponding Refs. Walsh et al. (2009), Shan and Chen (1993). In the following, only relevant parts that are necessary to understand the HMCSC are described. The full declaration of notations is also given in Appendix A.

The main equation of the HMCSC that combines the GS-WBS homogenization approach (Walsh et al., 2009) with the original MCSC and the Shan–Chen forcing scheme (Shan and Chen, 1993) is

$$
\begin{aligned}
f_{i,\sigma}\left(\mathbf{x}+\mathbf{c}_i \Delta t, t+\Delta t\right) = \quad & (1-n_{s,\sigma}(\mathbf{x}))f_{i,\sigma}(\mathbf{x},t) \\
& - (1-n_{s,\sigma}(\mathbf{x}))\frac{\Delta t}{\tau_\sigma}\left(f_{i,\sigma}(\mathbf{x},t)-f_{i,\sigma}^{\mathrm{eq}}(\mathbf{x},t)\right) \\
& + n_{s,\sigma}(\mathbf{x})f_{\bar{i},\sigma}\left(\mathbf{x},t^*\right).
\end{aligned}
\tag{1}
$$

Here, f_σ is the distribution function of the component σ, f_σ^{eq} is the Maxwell–Boltzmann equilibrium distribution function (cf. Eq. (A.3) in the Appendix), and τ_σ is the relaxation time. The last term in Eq. (1) corresponds to the bounce-back scheme. The parameter $n_{s,\sigma}$ comes from the homogenization approach. Originally it was called the solid fraction which is due to the intuitive interpretation of relating flow properties to the solid volume fraction. In the following, the same parameter is called the bounce-back fraction to highlight its technical origin and to prevent a misinterpretation. Note that the bounce-back fraction has to be chosen to retrieve the permeability and should be seen as a space-dependent, internal model parameter which is not necessarily directly proportional to the amount of solid material in a lattice cell. Its general relation to the permeability for a single-phase fluid (Walsh et al., 2009) is

$$
k = \frac{1-n_s}{2n_s}\nu\Delta t.
\tag{2}
$$

Similar to the MCSC (Shan and Chen, 1993), Eq. (1) is solved for each component σ involved in the multi-phase flow. Thus, all lattice cells are occupied by every component simultaneously. A cell belonging to component σ is composed of the main component density ρ_σ and the dissolved densities with $\rho_{\mathrm{dis}} \ll \rho_\sigma$. The fluid–fluid and solid–fluid interactions are incorporated as interaction forces via f_σ^{eq} (cf. Eq. (6)). They are physically motivated by a pseudopotential that similar to molecular dynamic simulations models molecular interactions to recover cohesion and adhesion, e.g., in wetting or transport processes (Lautenschlaeger and Hasse, 2019b,a; Diewald et al., 2020; Lautenschlaeger and Hasse, 2020).

The separation of component σ by another component $\bar{\sigma}$ is driven by a fluid–fluid interaction force $\mathbf{F}_{\mathrm{inter}}$

$$
\mathbf{F}_{\mathrm{inter},\sigma}(\mathbf{x}) = -\rho_\sigma(\mathbf{x})\,G_{\mathrm{inter},\sigma\bar{\sigma}}\sum_i w_i \rho_{\bar{\sigma}}\left(\mathbf{x}+\mathbf{c}_i\Delta t\right)\mathbf{c}_i\Delta t,
\tag{3}
$$

where the interaction parameter $G_{\mathrm{inter},\sigma\bar{\sigma}}$ determines the strength of the cohesion.

The wettability or adhesion of the component σ at a solid wall is modeled with the solid–fluid interaction force $\mathbf{F}_{\mathrm{ads},\sigma}$

$$
\mathbf{F}_{\mathrm{ads},\sigma}(\mathbf{x}) = -\rho_\sigma(\mathbf{x})\,G_{\mathrm{ads},\sigma}\sum_i w_i s\left(\mathbf{x}+\mathbf{c}_i\Delta t\right)\mathbf{c}_i\Delta t,
\tag{4}
$$

where the adhesion parameter $G_{\mathrm{ads},\sigma}$ determines the wetting behavior and s is an indicator function which is $s = n_{s,\sigma}$ here.

Table 1
Overview of the physical quantities of the system consisting of fluid 1 and fluid 2.
Values are given in LBM units (lu: length unit; ts: time step; mu: mass unit).

Density	$\rho_1 = \rho_2 = 0.99 \frac{mu}{lu^3}$
	$\rho_{dis,1} = \rho_{dis,2} = 0.01 \frac{mu}{lu^3}$
Kinematic viscosity	$\nu_1 = \nu_2 = 1.667 \cdot 10^{-1} \frac{lu^2}{ts}$
Surface tension	$\gamma = 7.68 \cdot 10^{-2} \frac{mu}{ts^2}$
Model parameters	$\tau_1 = \tau_2 = 1.0$
	$n_s = n_{s,1} = n_{s,2}$
	$G_{inter,12} = G_{inter,21} = 1.75$
	$G_{ads,2} = -G_{ads,1} = \frac{1}{4} G_{inter,12}(\rho_1 - \rho_{dis,2})\cos\theta$ (Huang et al., 2007)
	$\Delta \mathbf{x} = \Delta t = 1$

It was shown by Huang et al. (2007) how $G_{inter,\sigma\bar{\sigma}}$ and $G_{ads,\sigma}$ relate to the interfacial tension γ and the contact angle θ, respectively. It will be shown in Section 3, that the same parametrization can be used for the HMCSC, too, which underlines its physical consistency with the original MCSC.

Additional external forces $\boldsymbol{F}_{ext}$ which act on all components, such as gravity, are distributed to each component σ by their density ratios

$$\boldsymbol{F}_{ext,\sigma} = \frac{\rho_\sigma}{\rho} \boldsymbol{F}_{ext}, \tag{5}$$

where $\rho = \sum_\sigma \rho_\sigma$ is the total density of all components in a lattice cell.

All aforementioned force contributions are summarized to the total force $\boldsymbol{F}_{tot,\sigma} = \boldsymbol{F}_{inter,\sigma} + \boldsymbol{F}_{ads,\sigma} + \boldsymbol{F}_{ext,\sigma}$. Using the Shan–Chen forcing approach, $\boldsymbol{F}_{tot,\sigma}$ is finally incorporated into $\boldsymbol{f}_\sigma^{eq}(\rho_\sigma, \mathbf{u}_\sigma^{eq})$ (cf. Eq. (A.3) in the Appendix) as a force-induced equilibrium velocity shift of each component

$$\mathbf{u}_\sigma^{eq} = \frac{\sum_\sigma \rho_\sigma \mathbf{u}_\sigma / \tau_\sigma}{\sum_\sigma \rho_\sigma / \tau_\sigma} + \frac{\tau_\sigma \boldsymbol{F}_{tot,\sigma}}{\rho_\sigma}. \tag{6}$$

Note that the equilibrium velocity $\mathbf{u}^{eq}$ must not be confused with the macroscopic streaming velocity of the mixture. For the HMCSC, the latter is given by

$$\mathbf{u}_{macro} = \frac{1}{\rho} \sum_\sigma (1 - n_{s,\sigma}) \left(\sum_i f_{i,\sigma} \mathbf{c}_i + \frac{\boldsymbol{F}_{tot,\sigma} \Delta t}{2} \right), \tag{7}$$

where the factor $(1 - n_{s,\sigma})$ comes from the homogenization approach (Walsh et al., 2009; Yehya et al., 2015; Pereira, 2016).

3. Model validation

The HMCSC has been implemented in the open-source LBM tool *Palabos* (version 2.3) (Latt et al., 2021). This extended version of *Palabos* was used to test the HMCSC for typical porous media benchmark scenarios for single- and two-phase flow. The benchmark scenarios were chosen to cover a wide range of levels of complexity and are discussed in the following. All results are given in lattice units or dimensionless units and compared with analytical or semi-analytical solutions where available. Only 2D simulations were conducted for the validation. A 3D application of the HMCSC is described in Section 4. All relevant model parameters are given in Table 1. This default parameter setting represents a simple, clearly defined, frequently used, and relevant case, and is therefore most suitable to benchmark the HMCSC approach. Unless specified otherwise, it is used for all simulations of the present work. For studying single-phase flows using the HMCSC, the MCSC-related model parameters were set to zero, i.e. $G_{inter,\sigma\bar{\sigma}} = G_{ads,\sigma} = 0.0$. Under these conditions, the model reduces to the GS-WBS with Shan–Chen forcing scheme and no-slip boundary conditions at solids.

3.1. Permeability

The key parameter of the homogenization is the bounce-back fraction n_s. For GS-WBS it was shown to be related to the permeability k

following Eq. (2) (Walsh et al., 2009). It is shown in the following that Eq. (2) is also true when using the HMCSC for single-phase flows.

The simulation domain represents a fully homogenized porous medium, where n_s was identical in all lattice cells. The system was fully periodic, and its dimensions along the x- and y-direction were $H = 50$ lu each. The fluid flow was driven by the body force $\boldsymbol{F}_{ext} = 10^{-5}$ (mu lu)/ts^2 in $+x$-direction.

The permeability k was calculated using Darcy's law for a single-component fluid

$$k = \frac{\nu \langle \rho u \rangle}{F_{ext}}, \tag{8}$$

where $\langle \rho u \rangle$ is the average momentum in x-direction.

In addition, the relative permeabilities $k_{r,\sigma}$ were determined for a two-phase flow in the absence of adhesion $(G_{ads,\sigma} = 0.0)$

$$k_{r,\sigma} = \frac{k(S_\sigma)}{k(S_\sigma = 1.0)}. \tag{9}$$

Here, the index σ denotes fluid 1 or fluid 2, respectively. S_σ is the saturation of the simulation domain with fluid σ, and the right-hand side is the ratio between the permeability at a certain saturation S_σ with the corresponding single-phase permeability, i.e. $S_\sigma = 1.0$, both determined using Eq. (8).

For the single-phase flow, n_s was varied in the range $n_s = [0.0001, 0.9999]$. For the two-phase flow, exemplary values $(n_s = \{0.1, 0.5, 0.9\})$ were chosen, where for each value of n_s, S_σ was varied in the range $S_1 = 1 - S_2 = [0, 1]$.

Fig. 1(a) shows the simulation results and the analytical solution (cf. Eq. (2)) of k for the single-phase flow. They are in excellent agreement which confirms the consistency with the GS-WBS and the applicability of Eq. (2) for the HMCSC. Fig. 1(b) shows the simulation results of $k_{r,1}$ and $k_{r,2}$ for different n_s and as a function of S_1. Hardly any dependence on n_s was observed. The results follow an almost linear trend which is typical for fluids with low interfacial tension (Mu et al., 2019). Moreover, as both fluids have identical properties (cf. Table 1), it holds $k_{r,1}(S_1) = k_{r,2}(1 - S_1)$. However, note that also other realistic scenarios with more general shapes of permeability curves can be considered using the HMCSC, e.g. for different simulation setups or if the properties of the two fluids are not identical.

3.2. Darcy-Brinkman flow

A critical requirement for all homogenization approaches is that they recover Darcy–Brinkman-type flow behavior in porous media (Chen and Zhu, 2008; Zhu and Ma, 2013; Li et al., 2014; Yehya et al., 2015; Ginzburg, 2016; Pereira, 2016; Zhu and Ma, 2018; Ning et al., 2019), which is described by the Darcy-Brinkman equation

$$\frac{\nu_B}{\phi} \frac{\partial^2 u}{\partial x^2} + F_{ext} - \frac{\nu}{k} u = 0. \tag{10}$$

Here, ν_B is the effective Brinkman viscosity, ν is the viscosity of the fluid, F_{ext} is the driving force, and ϕ and k are the porosity and permeability of the porous medium, respectively.

The analytical solution of Eq. (10) depends on the choice of boundary conditions. Three Darcy-Brinkman flow types were studied and compared to their analytical solutions. The different variants were: (1) Poiseuille flow, (2) Couette flow, and (3) open boundary flow.

The overall simulation scenario is schematically shown in Fig. 2. It consisted of two stratified layers of porous media for which the permeabilities were independently adjusted by $n_{s,left}$ and $n_{s,right}$. The simulation domain had the dimensions H and L along the x- and y-directions, respectively. The flow was driven along the $+y$-direction either by applying constant velocities to the boundary cells or a body force F_{ext} to all lattice cells. At steady state, the velocity profile $u(x)$ was determined.
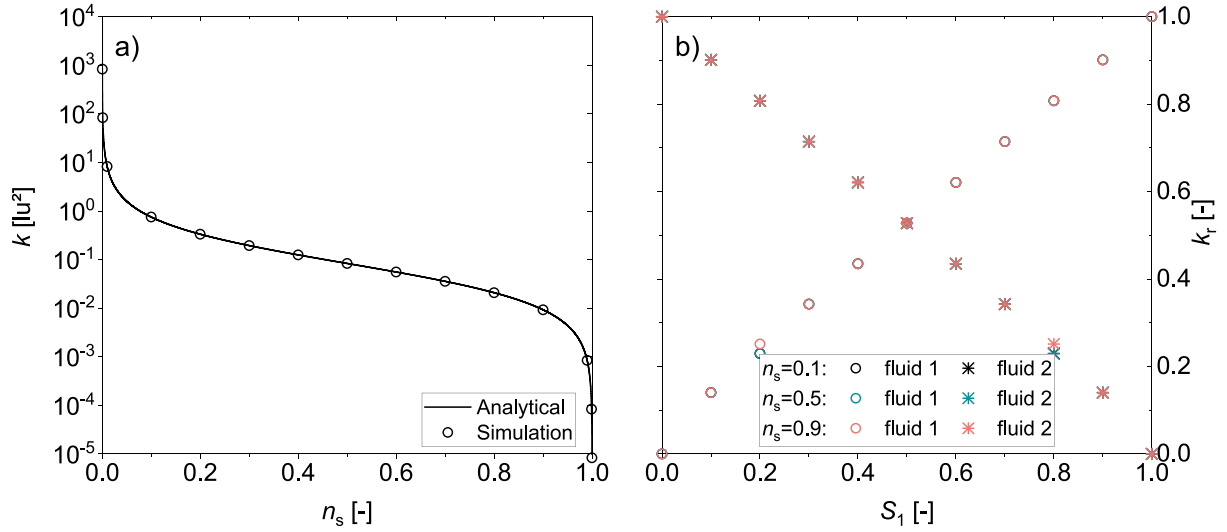
Fig. 1. Profiles of (a) the permeability k for single-phase flow and (b) the relative permeabilities k_r for two-phase flow as a function of n_s and the saturation S_1. The simulation results are denoted by the symbols. For k also the analytical solution (solid line, cf. Eq. (2)) is shown.
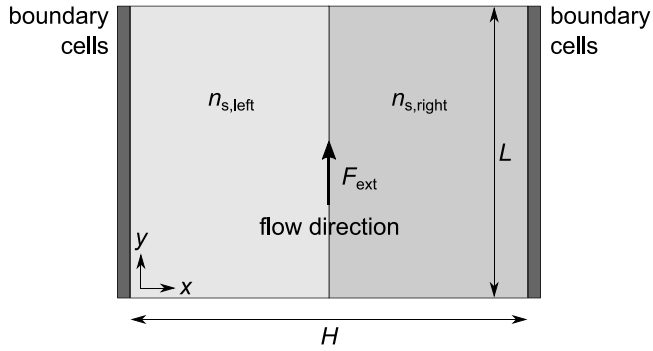

Fig. 2. Schematic simulation setup for Darcy–Brinkman-type flow phenomena. The dimensions of the channel along the x- and y-directions are H and L, respectively. The left ($x = [0, H/2]$, light gray) and the right ($x = [H/2, H]$, medium gray) half of the channel are filled with porous media defined by $n_{s,\text{left}}$ and $n_{s,\text{right}}$, respectively. The channel is bounded by boundary cells (dark gray) in the x-direction and has periodic boundaries in the y-direction. The flow is driven in $+y$-direction, e.g. by a body force F_{ext}.

Fig. 3. Velocity profiles of single-phase Darcy–Brinkman-type flow under Poiseuille conditions and at different bounce-back fractions n_s. The dimensions of the channel are $H = 50\,\text{lu}$ and $L = 50\,\text{lu}$. The flow is driven by the body force $F_{\text{ext}} = 10^{-5}\,(\text{mu}\,\text{lu})/\text{ts}^2$. Simulation results (circles) are shown together with their analytical solutions (solid lines, cf. Eq. (11)).

(1) Poiseuille flow. The Poiseuille flow was studied for a single-phase fluid in an homogeneous medium $\left(n_s = n_{s,\text{left}} = n_{s,\text{right}}\right)$ for which n_s was varied in the range $n_s = \{0.001, 0.01, 0.1, 0.5, 0.9\}$. No-slip boundary conditions were applied as bounce-back at the boundary cells. The dimensions and the body force were $H = 50\,\text{lu}$, $L = 50\,\text{lu}$, and $F_{\text{ext}} = 10^{-5}\,(\text{mu}\,\text{lu})/\text{ts}^2$, respectively. The analytical solution of Eq. (10) for this case is

$$u = \frac{F_{\text{ext}}\,k}{\nu}\left(1 - \frac{\cosh\left[r(x - H/2)\right]}{\cosh(rH/2)}\right), \qquad (11)$$

where $r = \sqrt{\nu\phi/k\nu_B} = \sqrt{2n_s/\nu}$ for $\phi = (1 - n_s)$ and $\nu_B = \nu$, and k was determined using Eq. (2).

Fig. 3 shows the simulation results and analytical solutions (cf. Eq. (11)) of the velocity profiles. They are in excellent agreement over a wide range of n_s, i.e. within Darcy $\left(\tilde{\sigma} = \text{Da}^{-0.5} = (k/H^2)^{-0.5} \gtrsim 100\right)$ and Brinkman ($100 \gtrsim \tilde{\sigma} \gtrsim 1$) regime.

(2) Couette flow. The Couette flow was also studied for a single-phase fluid in an homogeneous medium $\left(n_s = n_{s,\text{left}} = n_{s,\text{right}}\right)$ for which n_s was varied in the range of $n_s = \{0.001, 0.01, 0.1, 0.5, 0.9\}$ again. Velocity boundary conditions were applied to the boundary cells, i.e. $u(0) = 0\,\text{lu/ts}$ and $u(H) = U_0 = 0.01\,\text{lu/ts}$. The dimensions and the body force

were $H = 50\,\text{lu}$, $L = 50\,\text{lu}$, and $F_{\text{ext}} = 0\,(\text{mu}\,\text{lu})/\text{ts}^2$, respectively. The analytical solution of Eq. (10) for this case is given as

$$u = U_0 \frac{\sinh(rx)}{\sinh(rH)}, \qquad (12)$$

where again $r = \sqrt{2n_s/\nu}$.

Fig. 4 shows the simulation results and the analytical solutions (cf. Eq. (12)) of the velocity profiles. They are in excellent agreement within the Brinkman regime, i.e. for $n_s \leq 0.1$. For larger values of n_s, i.e. in the Darcy regime, deviations are observed close to the boundary cells $x/H \gtrsim 0.95$. This was also reported for other GS models and explained with an n_s-dependence of the no-slip conditions (Chen and Zhu, 2008; Zhu and Ma, 2013).
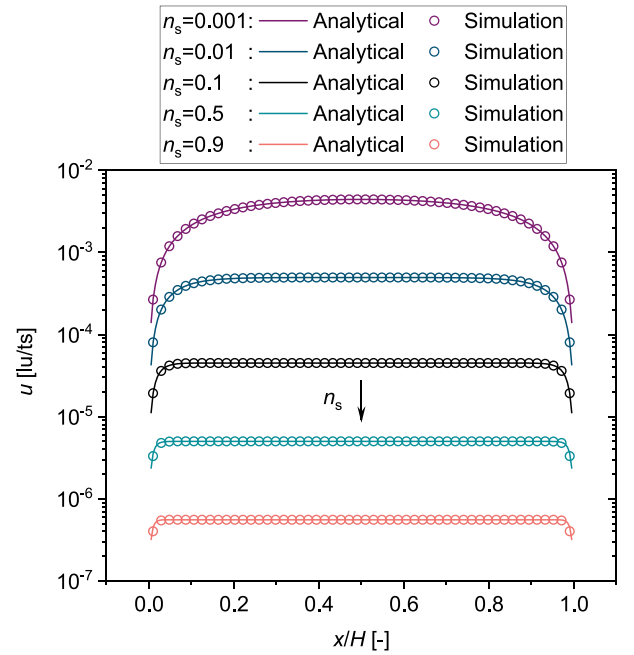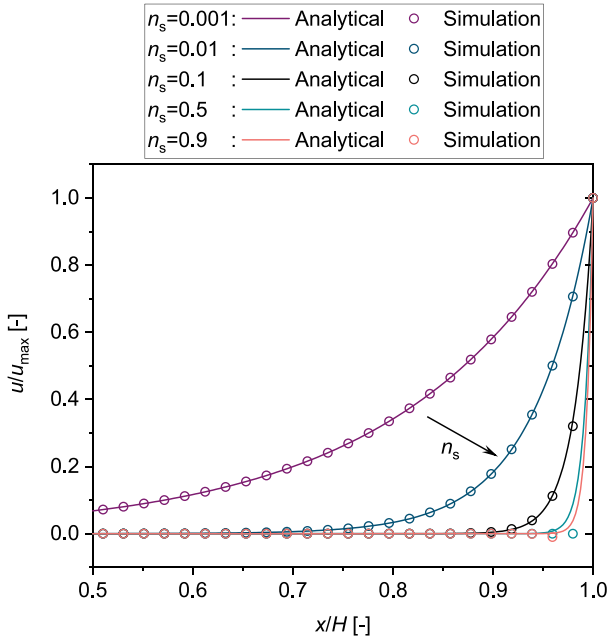
Fig. 4. Velocity profiles of single-phase Darcy–Brinkman-type flow under Couette conditions and at different bounce-back fractions n_s. The dimensions of the channel are $H = 50\,\text{lu}$ and $L = 50\,\text{lu}$. The flow is driven by the wall velocity $U_0 = u_{max} = 0.01\,\text{lu/ts}$. Simulation results (circles) are shown together with their analytical solutions (solid lines, cf. Eq. (12)).

Table 2
Declaration of the parameters from Eq. (13).

$U_{0,l} = \frac{k_l F_{ext}}{\nu}$	$U_{0,r} = \frac{k_r F_{ext}}{\nu}$
$p_l = \frac{k_r}{k_l}$	$p_r = \frac{k_l}{k_r}$
$q_l = \sqrt{\frac{n_{s,left}}{n_{s,right}}}$	$q_r = \sqrt{\frac{n_{s,right}}{n_{s,left}}}$
$r_l = \sqrt{\frac{2n_{s,left}}{\nu}}$	$r_r = \sqrt{\frac{2n_{s,right}}{\nu}}$

the results indicate that the HMCSC inherently overcomes an issue of the GS-WBS, which was reported by Zhu and Ma (2013) and Ginzburg (2016). They found that the GS-WBS in the formulation of Zhu and Ma (2013) revealed a non-physical velocity discontinuity at the interface for cases where $n_{s,left} \approx n_{s,right} \approx 1.0$. This was not observed here (cf. simulation with $n_{s,left} = 0.9$ and $n_{s,right} = 0.8$) and is assumed to be due to using the Shan–Chen forcing scheme in the present study (cf. Appendix B).

3.3. Bubble test

The interfacial tension γ is an inherent thermodynamic property that depends on the molecular interaction of a set of immiscible fluids as well as on the thermodynamic state of the system. Therefore, unlike in other GS models (McDonald and Turner, 2016; Pereira, 2016), it should not depend on the homogenization of a nanoporous medium. This is especially important, when the medium is heterogeneous, i.e. n_s is space-dependent. Thus, for each homogenized multi-phase LB model to be physically consistent, it has to be ensured that setting the model parameter $G_{inter,12}$ to a constant value for the whole simulation domain, does not lead to spatial variations of the interfacial tension.

This was verified using bubble tests. The simulation setup is shown in Fig. 6(a). The simulation domain consisted of an homogenized porous medium where all lattice cells had the identical bounce-back fraction n_s. The system was fully periodic. The dimensions of the simulation domain along the x- and y-direction were H. The system was initially filled with a bubble consisting of fluid 1 which was submersed in fluid 2. Both components had equal masses. The pressure difference between the center of the bubble and its surroundings, i.e. $\Delta p = p_1 - p_2$, as well as the bubble radius R were determined from the simulations. Therefrom, γ follows Laplace's law $\gamma = \Delta p R$. The influence of the parameters H, $G_{ads,1}$, n_s, and $G_{inter,12}$ on γ was studied. For the reference simulation case, the parameters were $H = 100\,\text{lu}$, $G_{ads,1} = 0.0$, $n_s = 0.5$, and $G_{inter,12} = 1.75$. Unless specified otherwise, the subsequent simulations used those default parameters.

Fig. 6(b) shows the results of γ for different values of H, $G_{ads,1}$, n_s, and $G_{inter,12}$. It was observed that γ does not depend on $G_{ads,1}$ and n_s. This was also confirmed for bubble spreading in structurally resolved porous media and is shown in Figure SI-1 in the Supporting Information. Thus, the interfacial tension was only affected by H and $G_{inter,12}$. For increasing H, γ decreased slightly and converged towards the asymptotic value $\gamma = 0.077\,\text{mu/ts}^2$. This was related to the imprecise determination of the bubble radius R for small systems, but worked well for $H \geq 100\,\text{lu}$. In contrast, the influence of the fluid–fluid interaction $G_{inter,12}$ on γ was large which was to be expected. γ increased with increasing $G_{inter,12}$. The results were in perfect agreement with the corresponding values reported by Huang et al. (2007). These were $\gamma = \{0.051, 0.078, 0.104\}\,\text{mu/ts}^2$ for $G_{inter,12} = \{1.50, 1.75, 2.00\}$, respectively. They were determined using the original MCSC, which corresponds to using the HMCSC for $n_s = 0$.

3.4. Washburn simulations

The Washburn equation (Washburn, 1921)

(3) Open boundary flow. The open boundary flow was studied for both a single-phase fluid and a two-phase fluid in an heterogeneous medium ($n_{s,left} \neq n_{s,right}$). The influence of adhesion was neglected ($G_{ads,\sigma} = 0.0$). In the left half of the domain a constant value $n_{s,left} = 0.9$ was chosen, while $n_{s,right}$ was varied in the range of $n_{s,right} = \{0.001, 0.01, 0.1, 0.5, 0.8\}$. Instead of the boundary cells, periodic boundary conditions along the x-direction were applied. The dimensions and the body force were $H = 100\,\text{lu}$, $L = 50\,\text{lu}$, and $F_{ext} = 10^{-6}\,(\text{mu lu})/\text{ts}^2$, respectively. In case of the two-phase flow, the system was initialized with fluid 1 in the left half ($x = [0, H/2]$) and fluid 2 in the right half of the domain ($x = [H/2, H]$). The piece-wise analytical solution of Eq. (10) for the open boundary flow is given as

$$u_l = U_{0,l}\left[1 - \frac{(1 - p_l)\cosh(r_l(x - \frac{H}{4}))}{\sinh(r_l \frac{H}{4})\left[q_l \coth(r_r \frac{H}{4}) + \coth(r_l \frac{H}{4})\right]}\right], \forall x \in [0, \frac{1}{2}H],$$

(13a)

$$u_r = U_{0,r}\left[1 + \frac{(p_r - 1)\cosh(r_r(\frac{3H}{4} - x))}{\sinh(r_r \frac{H}{4})\left[q_r \coth(r_l \frac{H}{4}) + \coth(r_r \frac{H}{4})\right]}\right], \forall x \in]\frac{1}{2}H, H].$$

(13b)

The corresponding parameters U_0, p, q, and r are given in Table 2. The labels 'l' and 'r' denote the left ($x = [0, H/2]$) and the right ($x =]H/2, H]$) half of the simulation domain, respectively.

Fig. 5 shows the simulation results for (a) the single-phase flow and (b) the two-phase flow as well as the corresponding analytical solutions (cf. Eq. (12)) for half the channel width only close to the interface ($x = [1/4, 3/4]H$). The results of the single-phase flow are in excellent agreement over a wide range of $n_{s,right}$, i.e. within Darcy and Brinkman regime. The results of the two-phase flow are also in good agreement with the analytical solutions. However, they are slightly overestimated for $n_{s,right} < 0.1$ due to slip at the interface. Moreover,

$$x_{inter} = \sqrt{\frac{\gamma \cos(\theta)}{2\eta}}\sqrt{R_{eff}\,t} = A\sqrt{B t},$$
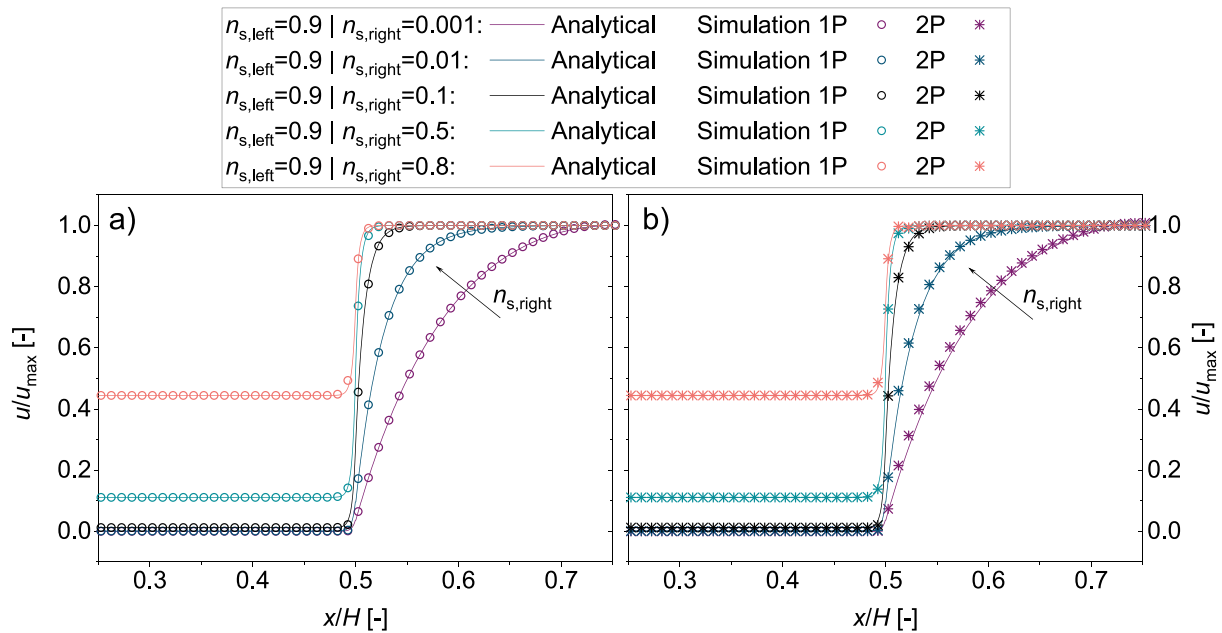
(14)

Fig. 5. Velocity profiles for (a) the single-phase and (b) the two-phase Darcy–Brinkman-type flow under open boundary conditions. The velocity is normalized by the maximum velocity $u_{\max}$ for which the numerical values are given in Table C.1 in Appendix A. The bounce-back fraction $n_{s,\text{left}}$ is kept constant at $n_{s,\text{left}} = 0.9$, while $n_{s,\text{right}}$ is varied in the range of $n_{s,\text{right}} = \{0.001, 0.01, 0.1, 0.5, 0.8\}$. The dimensions of the channel are $H = 100\,\text{lu}$ and $L = 50\,\text{lu}$. The flow is driven by the body force $F_{\text{ext}} = 10^{-6}\,(\text{mu\,lu})/\text{ts}^2$. Simulation results for single-phase (circles) and two-phase flow (asterisks) are shown together with their analytical solutions (solid lines, cf. Eq. (13)).
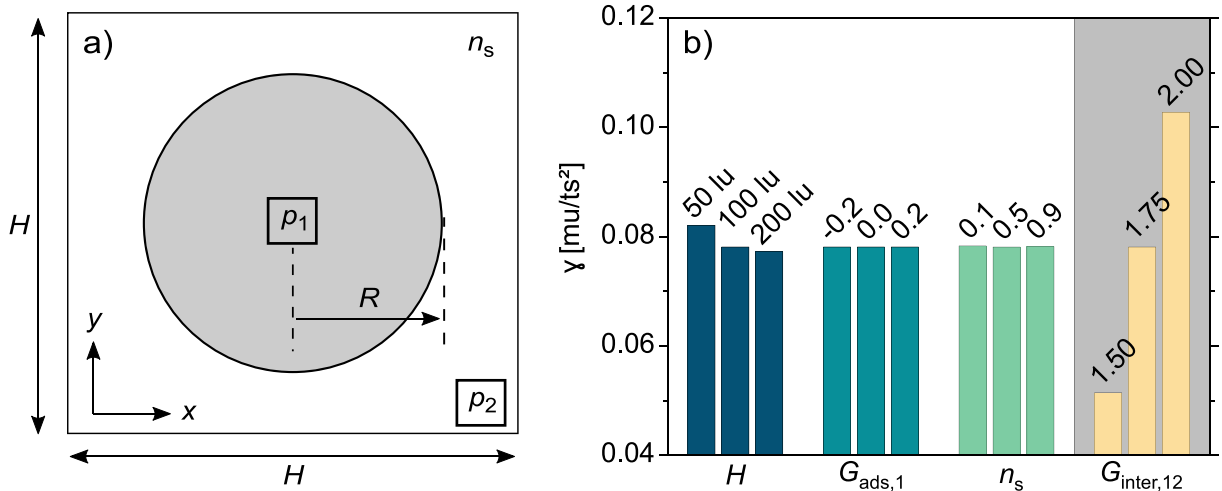

Fig. 6. Bubble test. (a) Simulation setup in which a bubble of fluid 1 (gray) is submersed in fluid 2 (white). The domain size is H along the x- and y-directions. The radius R and the pressures of both fluids, i.e. p_1 and p_2, were determined to calculate the interfacial tension γ. (b) Simulation results of γ as a function of different influencing factors, for which the specific values are given in the plot.

describes imbibition into homogeneous and isotropic porous media as 1D flow through a bundle of cylindrical tubes with effective radius R_{eff}. The position of the moving interface is denoted by x_{inter}. The equation is only valid if gravity is negligible (Das and Mitra, 2013; Li et al., 2015).

The flow is driven by the interplay of capillary forces and viscous forces, where the former depend on the interfacial tension γ and the contact angle θ, and the latter are determined by the dynamic viscosity of the fluid $\eta = \rho\nu$. The parameters A and B in Eq. (14) are fit parameters that are used in the following to fit the simulation data to the Washburn equation.

The simulation scenario consisted of a homogenized porous medium in which all lattice cells had the identical bounce-back fractions n_s. The system dimensions along the x- and y-direction were $H = 500\,\text{lu}$ and $L = 5\,\text{lu}$, respectively. The system was initially filled with fluid 2. The densities of fluid 1 and fluid 2 were prescribed at the inlet $\left(\rho_1(x = 0)\right)$

and outlet $\left(\rho_2(x = H)\right)$, respectively. Periodic boundary conditions were applied along the y-direction. Fluid 1 penetrated into the simulation domain in $+y$-direction and displaced fluid 2. The influence of the solid–fluid interaction and bounce-back fraction was studied. Correspondingly, the contact angle θ was varied by changing G_{ads} in the range of $G_{\text{ads}} = -G_{\text{ads},1} = [0.05, 0.40]$, and the permeability or effective radius R_{eff} was varied by changing n_s in the range of $n_s = \{0.1, 0.5, 0.9\}$.

Fig. 7 shows the simulation results for different values of G_{ads} and n_s. Results are given for $t \leq 5 \cdot 10^4$ ts. This corresponds to the Washburn regime $\left(x_{\text{inter}} \sim \sqrt{t}\right)$ where viscous effects dominate the flow (Das et al., 2012; Das and Mitra, 2013; Li et al., 2015). The data was used for fitting the Washburn equation Eq. (14).

For the simulations shown in Fig. 7(a), $n_s = 0.5$ and only G_{ads} was varied, while for the simulations in Fig. 7(b), $G_{\text{ads}} = 0.2$ and only n_s was varied. Correspondingly, for all fits in Fig. 7(a), parameter B was the
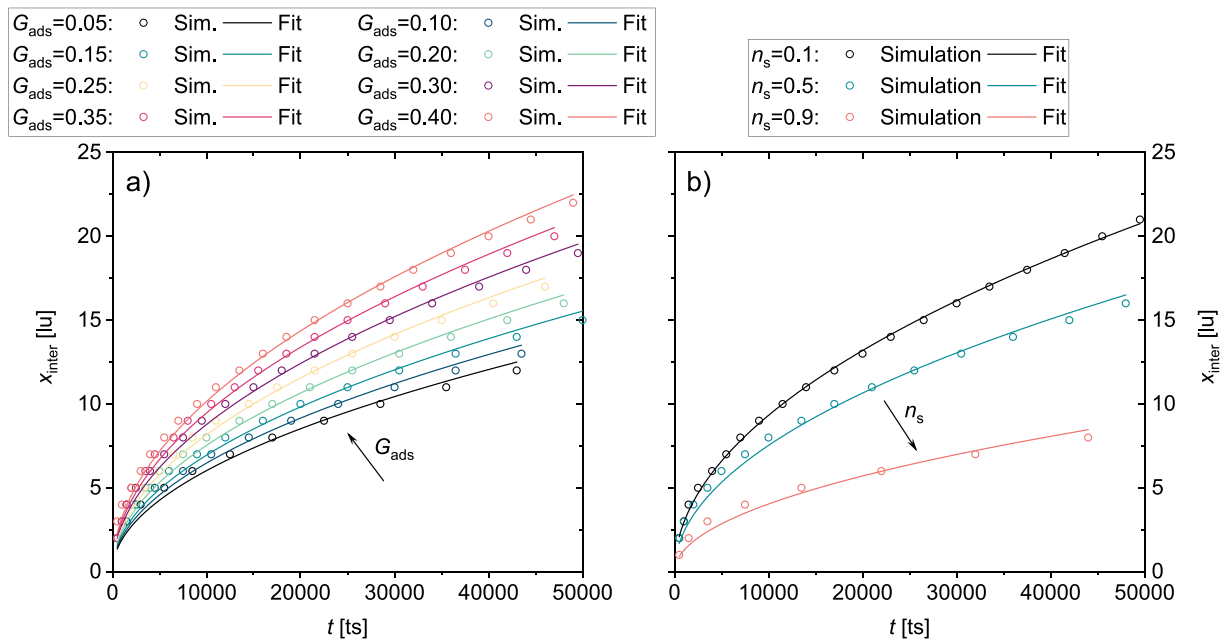
Fig. 7. Washburn simulations. Interface position x_{inter} as a function of time. The influence of (a) the solid–fluid interaction G_{ads} and (b) the bounce-back fraction n_{s} were studied. Simulation results (circles) are compared with fits to the analytical solutions of the Washburn equation (solid lines, cf. Eq. (14)) for which the parameters A and B are given in Table 3.

Table 3

Fit parameters A and B determined from the simulations (cf. Eq. (14)). The uncertainty of the fit is estimated by the corresponding coefficients of determination, i.e. R_A^2 and R_B^2, respectively. The data of θ and R_{eff} determined from the simulations using the Washburn equation Eq. (14) are given. They are compared to θ_{H} using the correlation by Huang et al. (2007) (cf. Eq. (15)).

G_{ads}	$A \left[\frac{\sqrt{\text{lu}}}{\sqrt{\text{ts}}}\right]$	R_A^2	θ [°]	θ_{H} [°]	n_{s}	B [lu]	R_B^2	R_{eff} [lu]
0.05	0.275	0.979	70.8	83.3	0.1	0.0737	0.999	0.0737
0.10	0.295	0.984	67.7	76.5	0.5	0.0481	0.990	0.0481
0.15	0.317	0.988	64.1	69.5	0.9	0.0138	0.972	0.0138
0.20	0.344	0.990	59.2	62.2				
0.25	0.373	0.992	52.9	54.3				
0.30	0.401	0.995	45.9	45.6				
0.35	0.432	0.996	36.0	35.3				
0.40	0.463	0.995	21.4	21.1				

same and only A was freely adapted. Vice versa for all fits in Fig. 7(b), A was fixed and only B was fitted to the simulations. Overall, the fits and the data are in good accordance. This is also confirmed by the large coefficients of determination, i.e. $R_A^2, R_B^2 > 0.97$.

The values for A and B as well as θ and R_{eff} are given in Table 3. In addition, θ determined from the Washburn simulations was compared with the correlation for the contact angle of Huang et al. (2007)

$$\cos(\theta_{\text{H}}) = \frac{4G_{\text{ads,2}}}{G_{\text{inter,12}}(\rho_1 - \rho_{\text{dis,2}})}, \qquad (15)$$

which was derived from sessile droplet simulations using the original MCSC. Interestingly, a good accordance of θ and θ_{H} was observed, especially for $\theta \in [0, 60]°$. For larger values of θ, the correlation slightly overestimated the simulation results. This was to some extent also observed in the paper of Huang et al. (2007) and is amplified by the increasing uncertainty of the fitting for $\theta > 60°$ (cf. R_A^2 in Table 3).

3.5. Porous obstacle flow

The last test concerned the simultaneous occurrence of free flow and Darcy-Brinkman flow. It followed an example of Spaid and Phelan (1998) which is also typically used as advanced benchmark in the literature (Yoshida and Hayashi, 2014; Silva and Ginzburg, 2015; Pereira, 2016).

The simulation scenario is shown in Fig. 8(a). It consisted of a channel with five circular porous obstacles with diameter $2R = 33$ lu from which the center-to-center distance was $D = 60$ lu. The dimensions of the system along the x- and y-direction were $L = 300$ lu and $H = 50$ lu, respectively. Periodic boundary conditions were applied along the y-direction. The system was initially filled with fluid 2. The densities of fluid 1 and fluid 2 were prescribed at the inlet $(\rho_1(x = 0))$ and outlet $(\rho_2(x = L))$, respectively. A body force $F_{\text{ext}} = 5 \cdot 10^{-5}$ (mu lu)/ts² in $+x$-direction was applied to both fluids, leading to fluid 1 penetrating into the simulation domain.

To ensure consistency with the simulations of Spaid and Phelan (1998), viscous effects of fluid 2 within the obstacles were neglected by setting $n_{\text{s,2}} = 0$ in all lattice cells of the domain. In contrast, $n_{\text{s,1}}$ was set to $n_{\text{s,1}} = \{0.1, 0.5, 0.9\}$ within the obstacles to account for the Darcy–Brinkman-type behavior of fluid 1 and to $n_{\text{s,1}} = 0$ for all other lattice cells. Thus, large viscosity ratios between the two fluids in the porous obstacles could be mimicked without running into numerical instabilities.

This scenario can be mathematically described by Darcy's law

$$\frac{\text{d}x_{\text{inter}}}{\text{d}t} = \frac{k_{\text{unsat}}}{\phi\eta}F_{\text{ext}}, \qquad (16)$$

where x_{inter} is the interface position, k_{unsat} is the permeability of the unsaturated system, ϕ is the effective porosity of the obstacles, η is the
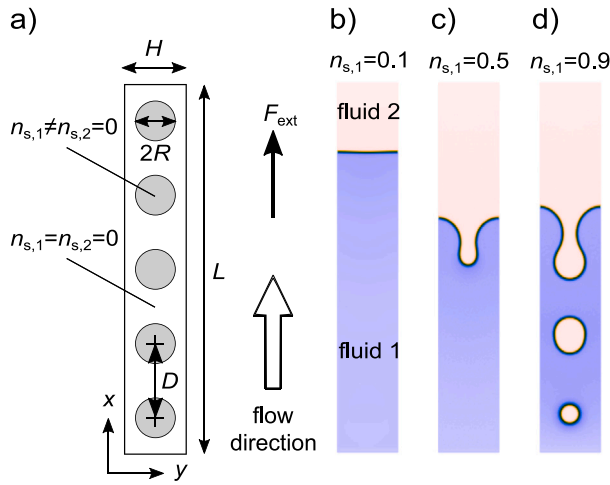
Fig. 8. Two-phase flow through a series of circular porous obstacles. (a) Schematic simulation setup. The dimensions along the *x*- and *y*-direction are L and H, respectively. The system contains five circular porous obstacles (gray shaded area) with radius R that are equidistantly distributed by the distance D. Within the obstacles $n_{s,1}$ is varied in the range of $n_{s,1} = \{0.1, 0.5, 0.9\}$. A body force F_{ext} is applied along the $+x$-direction. (b)-(d) Exemplary simulation results at different values of $n_{s,1}$. The snapshots show the distribution of fluid 1 (blue) and fluid 2 (red) at the time step $t = 50,000\,\text{ts}$ each.

Fig. 9. Interface position x_{inter} for a two-phase flow through a series of circular porous obstacles. Results are shown as a function of time t and $n_{s,1}$. Simulation results (solid lines) are compared with the fits to the analytical solutions (dashed lines, cf. Eq. (17)) for which k_{unsat} is given in Table 4.

Table 4
Comparison of unsaturated and saturated permeabilities, i.e. k_{unsat} and k_{sat}, respectively.

$n_{s,1}$	k_{unsat} [lu²]	k_{sat} [lu²]	k_{unsat}/k_{sat}
0.1	10.71	35.86	0.299
0.5	7.42	29.38	0.253
0.9	6.31	27.59	0.229

dynamic viscosity of fluid 1 and F_{ext} is the body force. The analytical solution of Eq. (16) is

$$x_{inter} = \frac{k_{unsat}}{\phi\eta}F_{ext}t, \qquad (17)$$

which was used to determine k_{unsat} from the simulations.

Representative snapshots of the simulations at $t = 50,000\,\text{ts}$ are shown in Fig. 8(b)-(d) for different values of $n_{s,1}$. They reveal that increasing $n_{s,1}$ retards the filling of the channel. For $n_{s,1} = 0.9$ even a distinct bubble or droplet formation within the porous obstacles was observed. These results agree qualitatively with results from the literature (Spaid and Phelan, 1998; Pereira, 2016).

Complementary, Fig. 9 shows quantitative simulation results and the corresponding fits to Eq. (17) for different values of $n_{s,1}$. The position of the interface was determined as $x_{inter} = L/2\big(S_1(y = 0) + S_1(y = H/2)\big)$, where the proportions of cells in the boundary and the center column of the simulation domain which were filled with fluid 1 were denoted $S_1(y = 0)$ and $S_1(y = H/2)$, respectively. The oscillations around the linear fits correspond to alternating deceleration and acceleration of the fluid front which depends on the varying width of the free-flow channel. The unsaturated permeabilities k_{unsat} were determined fitting Eq. (17) to the simulation data. The corresponding permeability of a saturated medium k_{sat} was determined following the lubrication theory of Phelan and Wise (1996).

Both k_{unsat} and k_{sat} are given in Table 4. The data shows that $k_{unsat} < k_{sat}$ and its ratio k_{unsat}/k_{sat} decreases for increasing $n_{s,1}$. These results are in qualitative agreement with simulative (Spaid and Phelan, 1998; Yoshida and Hayashi, 2014) and experimental (Parnas et al., 1995) observations.
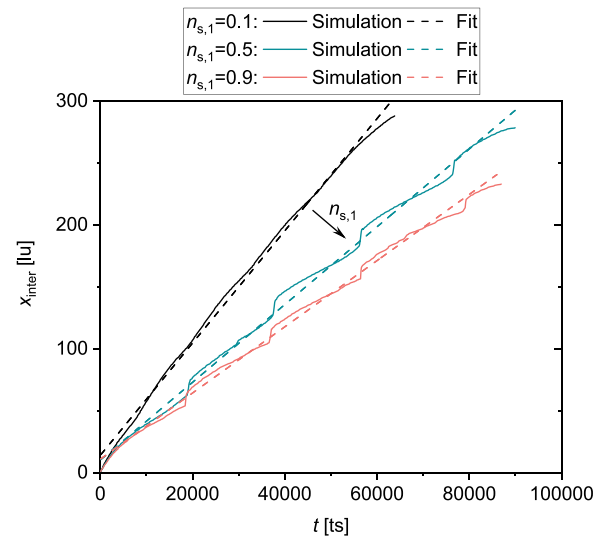
3.6. Numerical stability

Multi-component models in general are numerically stable for a limited range of density and viscosity ratios only (Krueger et al., 2016; Chen et al., 2014). Moreover, due to an imbalance of discretized forces especially at curved interfaces, they typically show spurious currents which can exacerbate the occurrence of numerical instabilities (Connington and Lee, 2012). Also the original MCSC on which the HMCSC is based is known to suffer from spurious currents (Connington and Lee, 2012; Chen et al., 2014). It is stable for a maximum density ratio of 2 as well as a maximum viscosity ratio of 5–10 (Kang et al., 2002a, 2004; Chen et al., 2014; Krueger et al., 2016). Remedies for those issues have been discussed in the literature (Shan, 2006; Sbragaglia et al., 2007; Connington and Lee, 2012; Chen et al., 2014), they were however not in the focus of this study.

To ensure that the coupling of MCSC and GS, i.e. the HMCSC, maintains the numerical stability characteristics of the original MCSC, the aforementioned two-phase flow benchmark scenarios from this section were conducted for different viscosity ratios $M = \nu_2/\nu_1$ and density ratios $G = \rho_1/\rho_2$. Thus, bubble tests, Washburn simulations, and porous obstacle flows were simulated using the same simulation setups and model parameters as described in the corresponding subsections, unless they are specified otherwise.

Washburn simulations were conducted for $M = 5$ ($G_{inter,12} = 2.75$, $G = 1$), $M = 10$ ($G_{inter,12} = 2.25$, $G = 1$), and $G = 2$ ($G_{inter,12} = 1.75$, $M = 1$). For each of the cases, n_s was varied in the range of $n_s = \{0.1, 0.5, 0.9\}$ and $G_{ads,1}$ was varied in the range of $G_{ads,1} = \{-0.2, 0.0, 0.2\}$. Porous obstacle simulations were conducted for the same parameter set while fixing $G_{ads,1} = 0.0$. For the bubble test the system was initialized close to mechanical equilibrium, i.e. $G = 1$, and the viscosity ratio ($M = \{5, 10\}$ with $G_{inter,12} = \{2.75, 2.25\}$, respectively) and $n_s = \{0.0, 0.1, 0.5, 0.9\}$ were varied.

All simulations, i.e. $M \leq 10$ and $G \leq 2$, were numerically stable. This is a strong indicator that the coupling of MCSC and GS via HMCSC has no negative effect on the numerical stability. In the following, exemplary results are shown for the bubble test scenario only. All other results are given in the Supporting Information.

Fig. 10 shows results of γ for $M = 5$ and $M = 10$ for different values of $G_{ads,1}$ and n_s each. It can be observed that γ does hardly depend on $G_{ads,1}$ and n_s. Thus, the interfacial tension is only affected by $G_{inter,12}$
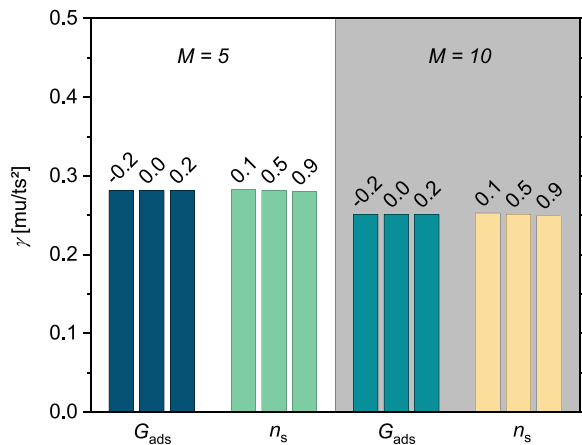
Fig. 10. Bubble test for different viscosity ratios M. Simulation results of γ as a function of different influencing factors, for which the specific values are given in the plot.

and the viscosities or τ, respectively. This is in agreement with the results shown in Fig. 6(b) for $M = 1$ and $G = 1$.

Also the spurious currents were analyzed for the bubble test scenario. Results are shown in Fig. 11 for $M = 1$ and $M = 5$. There, the results for $n_s = 0.0$ correspond to the original MCSC. It can be observed that larger viscosity ratios induce larger spurious currents and thus are numerically more unstable. This effect is however reduced when increasing n_s, i.e. decreasing the permeability of the porous medium (cf. Fig. 1(a)). When, e.g., increasing n_s from 0.0 to 0.9, the maximum velocity of spurious currents v_{max} is reduced by two orders of magnitude.

3.7. Discussion

In this section, the HMCSC was successfully validated using different single- and two-phase flow benchmark scenarios. Altogether, they demonstrate the broad applicability of the coupling approach presented here. Moreover, and just as important, it was shown that the HMCSC inherits all positive attributes and numerical stability characteristics from the original MCSC, the GS-WBS, and its multi-phase extension by Pereira (2016). At the same time, the HMCSC overcomes some deficiencies of these methods, i.e. non-physical discontinuities of interfacial tension and velocity at interfaces between different porous media. The features of the HMCSC are briefly summarized as follows:

1. As was shown by the bubble tests, the interfacial tension γ is independent of n_s and G_{ads}. Thus, the interfacial tension is a property of the fluids only and is not affected by the homogenization. This was also shown to be valid for viscosity ratios and density ratios above 1.
2. As was shown by the Washburn simulations, also the contact angle θ is independent of n_s. It is a property of the solid–fluid material combination only and is also not affected by the homogenization.
3. As was shown by the open boundary Darcy-Brinkman flow simulations, the HMCSC inherently ensures velocity continuity at interfaces of porous media with different n_s. No additional smoothing procedure as suggested by Yehya et al. (2015) is required.
4. The HMCSC is fully consistent with the original MCSC. Thus, the values for G_{ads} and G_{inter} can be chosen identical to the values that are used for the original MCSC. The same parametrization approach following the paper of Huang et al. (2007) as well as Eq. (15) can be applied to study the identical physical situations. No further parametrization is required.

5. The HMCSC is especially suitable for studying multi-phase flow in heterogeneous porous media where both the wetting properties and the permeability vary in space and time, while the physical properties of the fluid mixture are unaffected.
6. The HMCSC is accurate, intuitive, and easy to implement. Regarding its numerical stability, the HMCSC shows similar characteristics as the original MCSC, i.e. it is stable for density ratios up to 2 and viscosity ratios up to 5–10. Moreover, spurious currents can even be reduced when increasing n_s.

In contrast to most other GS models (Thorne and Sukop, 2004; Chen and Zhu, 2008; Zhu and Ma, 2013, 2018) including the model proposed by Pereira (2016) where forces were included using the Guo forcing scheme (Guo et al., 2002), the HMCSC uses the common Shan–Chen forcing scheme. Although, this leads to a τ-dependence of the viscosity (Yu and Fan, 2010; Silva and Ginzburg, 2015), it involves substantial advantages over the aforementioned models. The corresponding differences and their potential effects are briefly discussed in Appendix B.

4. Application and results

Practical applications of the HMCSC are most scenarios in which multi-phase fluid flow occurs in multi-scale porous media. In the context of hydrology, geoscience and petroleum engineering, the HMCSC can be especially interesting to study transport in pores, vugs and microfractures simultaneously, while also considering local changes of the permeability due to geochemical or biological processes. Thus, the HMCSC might be helpful to predict and gain insight into groundwater hydrology, geologic carbon storage and sequestration, and the recovery of oil and gas from different multi-scale porous rocks, such as sandstones, carbonates, and shale (Krevor et al., 2012; Ghezzehei, 2012; Mehmani et al., 2015; Soulaine et al., 2019; Mehmani et al., 2020; Hassannayebi et al., 2021).

However, as the research focus of our group is on energy storage materials, here the electrolyte filling of lithium-ion batteries was studied exemplarily. The pore sizes in such microstructures typically range from nano- to micrometers and its filling is not yet fully understood. Thus, it is of recent research interest with the objective to optimize the corresponding manufacturing process as well as the battery performance and lifetime (Wood et al., 2015; Weydanz et al., 2018).

A realistic 3D reconstruction of a lithium-ion battery cathode (Westhoff et al., 2018) with a porosity of $\phi_A = 40\%$ and neutral wetting conditions was used as a geometrical basis for all simulations. The filling of three variants of this structure was studied: (1) The pure electrode structure, (2) the electrode structure infiltrated with $V_B = 21\%$ volume fraction of a nanoporous binder, and (3) the electrode structure attached to a nanoporous and fully homogenized separator for which the generation is described in Appendix C.

The contact angles of the active material, binder, and separator were $\theta_A = 90°$, $\theta_B = 60°$, and $\theta_S = 90°$, respectively. They were converted to the model parameter $G_{ads,2} = -G_{ads,1}$ using Eq. (15). The bounce-back fractions in the homogenized porous media were $n_s = n_{s,1} = n_{s,2} = 0.5$ for the binder, while in the separator n_s was space-dependent and identical to the normalized grayscale value of each voxel of the separator image data.

Fig. 12 shows the schematic simulation setup where also the three different variants of microstructures are indicated. It is similar to the setup that was used in a recent study of our group (Lautenschlaeger et al., 2022) in which the electrolyte filling process was studied in very detail. Initially, the pore space was filled with gas only. Periodic boundary conditions were applied along the x- and z-direction. Along the y-direction an electrolyte reservoir and a gas reservoir were added at the inlet and outlet, respectively. The reservoirs had a thickness of four layers each in which the density of both fluids was prescribed.
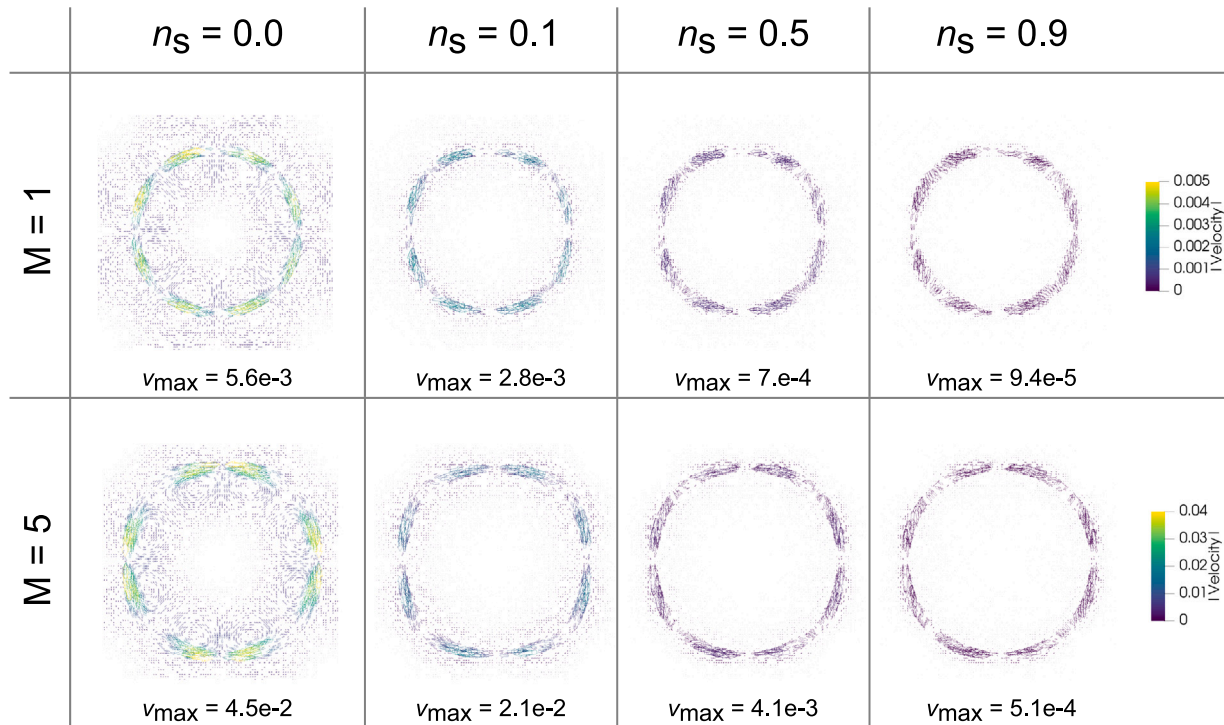
Fig. 11. Spurious currents during bubble tests using the HMCSC for different viscosity ratios M and bounce-back fractions n_s. The sizes of arrows in the velocity field are scaled by the corresponding $v_{\max}$. The color code is given by the legend on the right for which the units are lu/ts.
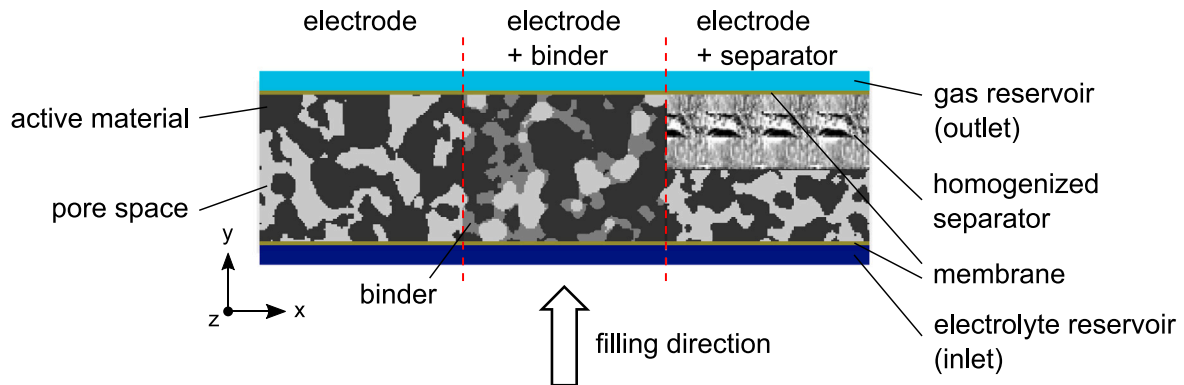

Fig. 12. Simulation setup schematically shown for the three different electrode structures. The pure electrode (left) consists of active material (black) and mesoscopic pore space (light gray) only. For the variant with binder (middle), the binder (darker gray) is infiltrated into this pore space. For the variant with separator (right), the separator (grayscale reconstruction) replaces the upper half of the electrode. The reservoirs in which the densities of electrolyte and gas are prescribed are marked in blue and cyan, respectively. The semi-permeable membranes adjacent to the reservoirs are depicted in yellow.

The initial electrolyte density at the inlet was ρ_1 and was incrementally increased during the simulation run. The gas density at the outlet was constant, i.e. ρ_2. Thereby, a pressure difference between the two fluids was applied to drive the electrolyte imbibition (cf. Eq. (18)). Between the reservoirs and the microstructures semi-permeable membranes were placed to prevent an unwanted fluid breakthrough. The inlet membrane was permeable for the electrolyte only. The outlet membrane was permeable for the gas only. This approach is in accordance with imbibition experiments and simulations that are typically used to analyze porous media in the context of geoscience or energy storage materials (Gostick et al., 2008; Karpyn et al., 2009; Pini et al., 2012; Krevor et al., 2012; Zhao et al., 2015; Danner et al., 2016; Tavangarrad et al., 2019; Zhu et al., 2021; Lautenschlaeger et al., 2022).

The model parameters for the simulations are given in Table 1, where fluid 1 and fluid 2 correspond to electrolyte and gas, respectively.

From each simulation, pressure–saturation curves were determined. They are a characteristic property of porous media and relate the pressure difference Δp needed for the imbibition to the amount of electrolyte in the pore space, i.e. the saturation S_1.

The pressure difference Δp was determined as

$$\Delta p = \langle p \rangle_{\text{inlet}} - \langle p \rangle_{\text{outlet}} \,, \tag{18}$$

where p was evaluated using Eq. (A.6), and $\langle p \rangle$ denotes the average pressure in the inlet and outlet reservoirs. The electrolyte saturation S_1 was determined as

$$S_1 = \frac{N_{\text{pore}}(\rho_1 \geq 0.5) + (1 - n_s)N_{\text{hom}}(\rho_1 \geq 0.5)}{N_{\text{pore}} + (1 - n_s)N_{\text{hom}}}, \tag{19}$$
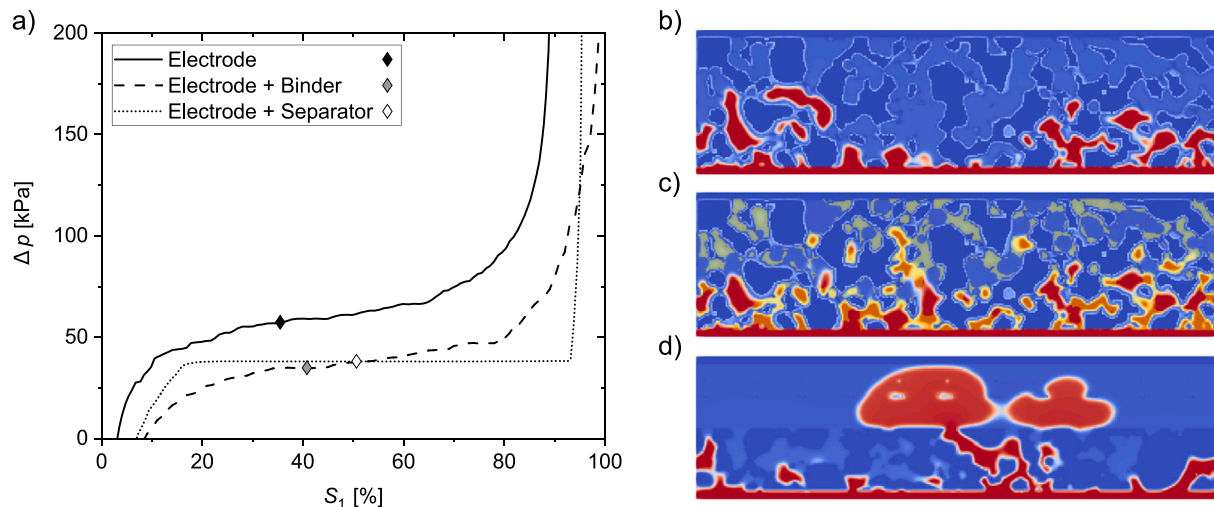
a)

Fig. 13. Electrolyte filling of electrode structures. (a) Pressure-saturation behavior of the pure electrode (solid line), the electrode with binder (dashed line), and the electrode attached to the separator (dotted line). The hashes denote the state at time step $t = 400,000$ ts for which snapshots are shown on the right. (b)-(d) Snapshots of cross sections in the xy-plane at $t = 400,000$ ts for (b) the pure electrode, (c) the electrode with binder, and (d) the electrode attached to the separator. The active component is depicted dark blue, the gas is depicted blue, the electrolyte is depicted red, and the binder is depicted yellow.

where the denominator and numerator correspond to the total pore space and the pore space in which $\rho_1 \geq 0.5\,\text{mu/lu}^3$, respectively. The number of pore lattice cells in the electrode structures and the homogenized nanoporous components are denoted by N_{pore} and N_{hom}, respectively. The latter were multiplied by the effective fluid fraction $(1 - n_s)$. Note, that for the calculation of the saturation only the lattice cells between the two membranes were considered.

A simulation run consisted of approximately 1,000,000 time steps. The pressure difference and the saturation were determined every 10,000 time steps during the production run. The simulations stopped when a further saturation was not possible and led to a steep increase of Δp.

Fig. 13(a) shows the pressure-saturation curves for the three different microstructures. They follow a sigmoidal behavior which is typically observed in the literature and can be explained based on the Young–Laplace equation. For all cases, the final saturation $S_{1,\text{final}}$ deviated from the theoretical optimum of 100% which indicates residual gas being entrapped in the pore space (Weydanz et al., 2018; Sauter et al., 2020).

A remarkable influence of the homogenized microstructures was observed. Compared to the pure electrode, the pressure-saturation curve for the electrode with binder shows a similar qualitative behavior, but appears to be shifted by $\Delta p < 0$ and $S_1 > 0$. Thus, by infiltrating a binder, the characteristics of the pore space were largely maintained. Only the enhanced wetting of the binder facilitated the electrolyte imbibition, led to a reduction of Δp and increased $S_{1,\text{final}}$ close to 100%. The pressure-saturation curve for the electrode attached to the separator shows a stronger influence as also the proportion of homogenized medium was larger compared to the structurally resolved electrode. For $S_1 < 15\%$, it behaves similar to the pure electrode, but is shifted by $S_1 > 0$. This similarity is because the electrolyte had not yet reached the separator, but was influenced by the pure electrode only. At larger saturations, a pressure plateau is reached which was also observed in the literature (Tavangarrad et al., 2019; Sauter et al., 2020). Here, it corresponds to the smooth filling of the fully homogenized separator. Along this plateau, the pressure increased by 0.4 kPa only, while at the end of the filling, a large pressure increase was observed due to the electrolyte imbibition into the small pores of the electrode. However, a notable gas entrapment remains. Note that in general, the shift along $S_1 > 0$ for the homogenized microstructures was also influenced by the definition of the saturation (cf. Eq. (19)), where adding lattice cells with a bounce-back fraction $n_s \neq 0$ led to a reduction of the total pore space.

Fig. 13(b)-(d) show snapshots of simulation cross sections (xy-plane) at $t = 400,000$ ts for the three different microstructures. The corresponding state points on the pressure-saturation curves are indicated by the hashes in Fig. 13(a). Compared to the pure electrode (cf. Fig. 13(b)), in Fig. 13(c) slightly more electrolyte is imbibed into pores with binder. Fig. 13(d) shows the electrolyte distribution in the resolved electrode and the homogenized separator. While the electrode part is not yet completely filled, a breakthrough of the electrolyte into the separator is observed. This state corresponds to the pressure plateau shown in Fig. 13(a). Moreover, Fig. 13(d) indicates some interesting model-related phenomena. On the one hand, the heterogeneity of n_s values in the separator can be used to mimic structural effects that influence gas entrapment, the flow orientation and deformation of the electrolyte-gas interface. On the other hand, and even more importantly, the interface thickness in the homogenized separator is constant and not affected by the distribution of n_s. It is also identical to the interface thickness in the structurally resolved pores for which $n_s = 0$.

Similar simulations were conducted by a different research group in an earlier study (Pereira, 2019) for a two-phase flow ($G = 1$, $M = 1$) in a tight sandstone sample composed of different partially permeable minerals using the approach of Pereira (2016). The results there confirm that Pereira's method has deficiencies with respect to discontinuities of properties in heterogeneous porous media. More specifically, Figures 7 and 8 in Pereira (2019) show strong density variations within the invading fluid phase. This is most likely a model artifact and related to a non-physical diverging interface thickness in the partially permeable regions.

In contrast, the simulation results of the current study determined using the HMCSC do not show such density variations. This gives further evidence of the potential and strength of the HMCSC. Moreover, it demonstrates possible applications of multi-phase flows in heterogeneous porous media going beyond electrochemical energy storage showcased in this work.

5. Conclusion

A simple but effective lattice Boltzmann approach was presented which is especially useful for the simulation of multi-phase flows in heterogeneous porous media, but can also be used to study single-phase flows. It follows the approach of Pereira (2016) and combines the grayscale method of Walsh et al. (GS-WBS) (Walsh et al., 2009), i.e. a homogenization approach, with the multi-component Shan–Chen

model (MCSC) (Shan and Chen, 1993). Therefore, it was called the homogenized multi-component Shan–Chen method (HMCSC).

The HMCSC was tested using a broad variety of benchmark scenarios that are typically used to validate single- and two-phase flow phenomena in porous media. The results were compared to analytical and semi-analytical solutions where available and shown to agree well. In addition, the HMCSC was applied to study the electrolyte filling of different variants of a realistic 3D reconstruction of a lithium-ion battery microstructure. Hereby, the HMCSC was shown to reproduce the relevant physical phenomena also within the homogenized nanoporous binder and separator. For example, including the wetting binder led to a reduction of the capillary pressure and an improvement of the final degree of saturation which is beneficial for the battery performance. Moreover, when adding the fully homogenized separator with space-dependent n_s values, structural effects which influence gas entrapment, characteristic flow paths, and the deformation of the electrolyte-gas interface were mimicked appropriately.

The HMCSC brings together the physical as well as numerical characteristics of GS-WBS and MCSC, i.e. it is applicable to immiscible fluids with viscosity ratios of up to 5–10. In addition, it overcomes some deficiencies of GS-WBS as well as the model reported by Pereira (2016) which are related to discontinuities of properties in heterogeneous porous media. In contrast to the aforementioned methods, the HMCSC is consistent with the original MCSC. This means, the MCSC-related model parameters G_{ads} and G_{inter} can be chosen identically to the parameters in the original MCSC (cf. Huang et al. (2007)). The corresponding physical properties, i.e. contact angle and interfacial tension, are not affected by the homogenization. They are constant and properties of the fluid only, even in heterogeneous porous media where n_s is space-dependent. Thus, no further parametrization is required. Moreover, in contrast to the GS-WBS, no artificial force and velocity discontinuity was observed at interfaces between different porous media. We assume that this is due to the Shan–Chen forcing scheme that was used for the HMCSC.

Altogether, the HMCSC is physically motivated, accurate, and efficient. Nonetheless, it is simple, intuitive, easy to implement, and allows a straightforward parametrization that is consistent with the original MCSC. Moreover, the HMCSC shows similar numerical stability characteristics. The results are promising and give cause to believe that techniques which alleviate limitations of the original MCSC are equally applicable to the HMCSC. By the right choice of model parameters, the HMCSC can be applied to all situations for which either the original MCSC or the GS-WBS can be used. However, the HMCSC is not restricted to these particular applications. All other research fields where multi-phase fluid flow occurs in heterogeneous and multi-scale porous media can benefit from this method, too. Potential applications are subsoil or groundwater flow (Pereira, 2016; Ning et al., 2019), oil recovery via water injection (Spaid and Phelan, 1998; Welge, 1952), biofilm growth in porous structures (Jung and Meile, 2021), the characterization of gas diffusion electrodes (Danner et al., 2016), water transport in gas diffusion layers (Zhu et al., 2021), or electrolyte filling of batteries (Shodiev et al., 2021; Lautenschlaeger et al., 2022).

CRediT authorship contribution statement

Martin P. Lautenschlaeger: Conceptualization, Investigation, Methodology, Software, Validation, Visualization, Writing – original draft. **Julius Weinmiller:** Validation, Writing – review & editing. **Benjamin Kellers:** Formal analysis, Writing – review & editing. **Timo Danner:** Conceptualization, Writing – review & editing. **Arnulf Latz:** Funding acquisition, Writing – review & editing.

Declaration of competing interest

The authors declare that they have no known competing financial interests or personal relationships that could have appeared to influence the work reported in this paper.

Data availability

Data will be made available on request.

Appendix A. Lattice Boltzmann method

LBM solves the discretized Boltzmann equation

$$f_i\left(\mathbf{x} + \mathbf{c}_i \Delta t, t + \Delta t\right) = f_i(\mathbf{x}, t) - \frac{\Delta t}{\tau}\left(f_i(\mathbf{x}, t) - f_i^{eq}(\mathbf{x}, t)\right), \quad (A.1)$$

using discrete distribution functions f_i, also referred to as populations. This approach uses the BGK collision (Bhatnagar et al., 1954), which describes the relaxation of f towards the Maxwell–Boltzmann equilibrium distribution function f^{eq} (cf. Eq. (A.3)) with a characteristic relaxation time τ. The relaxation time determines the kinematic viscosity via $\nu = c_s^2(\tau - 1/2\Delta t)$, where c_s^2 is the velocity set dependent lattice speed of sound.

The discretization of Eq. (A.1) is done in velocity space on a regular square or cubic lattice, for 2D and 3D, respectively. Each lattice cell is linked to its adjacent neighbors, denoted with i. The resulting velocity sets, $\mathbf{c}$, are called D2Q9 and D3Q27, which is often reduced to D3Q19 for efficiency, and are given in Eqs. (A.7) & (A.8). For completeness, t and $\mathbf{x}$ denote time and lattice location, with Δt and Δx being the temporal and spatial step. For the non-dimensional computationally efficient form, Δx and Δt are unity. As such they are usually omitted, but are included in this work for clarity and dimensional consistency.

The homogenization approach by Walsh et al. (2009) is

$$
\begin{aligned}
f_i\left(\mathbf{x} + \mathbf{c}_i \Delta t, t + \Delta t\right) = \quad & (1 - n_s(\mathbf{x})) f_i(\mathbf{x}, t) \\
& - (1 - n_s(\mathbf{x})) \frac{\Delta t}{\tau}\left(f_i(\mathbf{x}, t) - f_i^{eq}(\mathbf{x}, t)\right) \\
& + n_s(\mathbf{x}) f_{\bar{i}}\left(\mathbf{x}, t^*\right).
\end{aligned}
\quad (A.2)
$$

Here, $n_s \in [0, 1]$ acts as an interpolation factor that scales the fluid and solid behavior of f. From all populations f in a lattice cell, the fraction $(1 - n_s)$ is allowed to flow freely and therefore behaves fluid-like (cf. first and the second line of Eq. (A.2)), while the fraction n_s is bounced back and therefore behaves solid-like (cf. third line of Eq. (A.2)). The latter term uses the pre-collision populations which is highlighted by t^*. The symbol $\bar{i}$ denotes the direction opposite to i with the exception $i = 0 = \bar{i}$. Note that for $n_s = 0$, Eq. (A.2) is equivalent to the default LB BGK equation that describes pure fluid flow, Eq. (A.1), while for $n_s = 1$ it corresponds to pure bounce-back that describes a no-slip wall.

The MCSC approach has been fully covered in Section 2. It is iterated that for each component σ used, a unique discrete population function f_σ is needed. Therefore, in the following σ is explicitly mentioned in all equations.

A.1. Maxwell–Boltzmann distribution

The Maxwell–Boltzmann equilibrium distribution function is given by

$$f_{i,\sigma}^{eq} = w_i \rho_\sigma \left[1 + \frac{\mathbf{c}_i \mathbf{u}_\sigma^{eq}}{c_s^2} + \frac{(\mathbf{c}_i \mathbf{u}_\sigma^{eq})^2}{2c_s^4} - \frac{\mathbf{u}_\sigma^{eq} \mathbf{u}_\sigma^{eq}}{2c_s^2} \right]. \quad (A.3)$$

Here, w_i are the lattice specific weights, ρ_σ is the fluid density of component σ (cf. Eq. (A.4)) and $\mathbf{u}^{eq}$ is the equilibrium velocity (cf. Eq. (6)).

$$[\mathbf{c}_0, \mathbf{c}_1, \mathbf{c}_2, \mathbf{c}_3, \mathbf{c}_4, \mathbf{c}_5, \mathbf{c}_6, \mathbf{c}_7, \mathbf{c}_8, \mathbf{c}_9, \mathbf{c}_{10}, \mathbf{c}_{11}, \mathbf{c}_{12}, \mathbf{c}_{13}, \mathbf{c}_{14}, \mathbf{c}_{15}, \mathbf{c}_{16}, \mathbf{c}_{17}, \mathbf{c}_{18}] \tag{A.8}$$

$$= \frac{\Delta x}{\Delta t} \begin{bmatrix} 0 & -1 & 0 & 0 & -1 & -1 & -1 & -1 & 0 & 0 & 1 & 0 & 0 & 1 & 1 & 1 & 1 & 0 & 0 \\ 0 & 0 & -1 & 0 & -1 & 1 & 0 & 0 & -1 & -1 & 0 & 1 & 0 & 1 & -1 & 0 & 0 & 1 & 1 \\ 0 & 0 & 0 & -1 & 0 & 0 & -1 & 1 & -1 & 1 & 0 & 0 & 1 & 0 & 0 & 1 & -1 & 1 & -1 \end{bmatrix}$$

Box I.

A.2. Multi-phase physical quantities

The macroscopic physical quantities can be recovered from the discrete distribution function. In the following they are expressed in terms of multiple phases, but apply for single-phase fluids as well.

The fluid density of component σ is the zeroth moment of $\mathbf{f}_\sigma$ and determined as

$$\rho_\sigma = \sum_i f_{i,\sigma}. \tag{A.4}$$

The velocity of component σ is the first moment of $\mathbf{f}_\sigma$ and determined as

$$\mathbf{u}_\sigma = \frac{1}{\rho_\sigma} \sum_i f_{i,\sigma} \mathbf{c}_i. \tag{A.5}$$

The total pressure p of the mixture follows the ideal gas law. It is extended by a contribution from the fluid–fluid interaction which is especially relevant at the interface. p is determined as

$$p(\mathbf{x}) = c_s^2 \left[\rho(\mathbf{x}) + G_{\text{inter},\sigma\bar{\sigma}} \rho_\sigma(\mathbf{x}) \rho_{\bar{\sigma}}(\mathbf{x}) \Delta t^2 \right]. \tag{A.6}$$

A.3. Velocity sets

The HMCSC has been implemented for both 2D and 3D simulations. The corresponding velocity sets used for the simulations of the present work, i.e. D2Q9 and D3Q19, are given in the following:

D2Q9

$$[\mathbf{c}_0, \mathbf{c}_1, \mathbf{c}_2, \mathbf{c}_3, \mathbf{c}_4, \mathbf{c}_5, \mathbf{c}_6, \mathbf{c}_7, \mathbf{c}_8] \tag{A.7}$$

$$= \frac{\Delta x}{\Delta t} \begin{bmatrix} 0 & -1 & -1 & -1 & 0 & 1 & 1 & 1 & 0 \\ 0 & 1 & 0 & -1 & -1 & -1 & 0 & 1 & 1 \end{bmatrix}$$

The D2Q9 weights are: $w_i = 4/9$ for $|\mathbf{c}_i| = 0$, $w_i = 1/9$ for $|\mathbf{c}_i| = 1$, and $w_i = 1/36$ for $|\mathbf{c}_i| = \sqrt{2}$ with the speed of sound $c_s = 1/\sqrt{3}\Delta x/\Delta t$.

D3Q19

See Box I. The D3Q19 weights are: $w_i = 1/3$ for $|\mathbf{c}_i| = 0$, $w_i = 1/18$ for $|\mathbf{c}_i| = 1$, and $w_i = 1/36$ for $|\mathbf{c}_i| = \sqrt{2}$ with the speed of sound $c_s = 1/\sqrt{3}\Delta x/\Delta t$.

Appendix B. Guo vs. Shan–chen forcing

It has been reported in literature (Zhu and Ma, 2013; Yehya et al., 2015; Ginzburg, 2016) and also mentioned in the main text of this paper, that using the GS-WBS can result in velocity discontinuities at interfaces between different porous media. This was not observed when using the HMCSC (cf. Fig. 5). The reason might be due to the fact that the HMCSC uses the Shan–Chen forcing scheme (Shan and Chen, 1993), while the Guo forcing scheme (Guo et al., 2002) was used for the simulations reported in Zhu and Ma (2013), Ginzburg (2016).

The differences between both forcing schemes are briefly outlined in the following. For brevity regarding the notation, the position $\mathbf{x}$ is omitted and the time step is indicated in the exponent. The meaning of which is: t is the current time step, and $\tilde{t}$ denotes the state just before streaming. To emphasize and avoid confusion, t^* is used in addition to denote the pre-collision state.

Table C.1
Numerical values of the maximum velocities u_{max} that were used to normalize the velocity profiles in Fig. 5.

$n_{s,2}$	u_{max} [lu/ts]
0.001	$4.732 \cdot 10^{-4}$
0.01	$4.948 \cdot 10^{-5}$
0.1	$4.500 \cdot 10^{-6}$
0.5	$5.000 \cdot 10^{-7}$
0.8	$1.250 \cdot 10^{-7}$

$$\text{GS} - \text{WBS}: f_i^{\tilde{t}} = \quad (1 - n_s) f_i^t - (1 - n_s) \frac{\Delta t}{\tau} \left(f_i^t - f_i^{\text{eq},t}(\mathbf{u}_{\text{macro}}) \right) + n_s f_{\tilde{i}}^{t^*}$$

$$\tag{B.9}$$

$$+ (1 - n_s) F_i(\mathbf{F}_{\text{tot}}, \mathbf{u}_{\text{macro}})$$

$$\text{HMCSC}: f_i^{\tilde{t}} = \quad (1 - n_s) f_i^t - (1 - n_s) \frac{\Delta t}{\tau} \left(f_i^t - f_i^{\text{eq},t}(\mathbf{u}^{\text{eq}}) \right) + n_s f_{\tilde{i}}^{t^*}$$

$$\tag{B.10}$$

Eqs. (B.9) & (B.10) show the GS-type LB BGK equation in the Guo and Shan–Chen forcing scheme, respectively. The most obvious difference between both is the force term F_i in Eq. (B.9). It is directly dependent on the total force $\mathbf{F}_{\text{tot}}$. The whole term is scaled by the factor $(1 - n_s)$. This means that also the fluid–fluid and solid–fluid force contributions are scaled by $(1 - n_s)$ leading to an n_s-dependent interfacial tension and wetting behavior which was shown to be circumvented when using the HMCSC. Moreover, at the interface between two porous media from which the n_s values differ, the force term is also scaled differently, which might be one reason for the force and velocity discontinuity observed in the literature (Zhu and Ma, 2013; Yehya et al., 2015; Ginzburg, 2016).

Another might be that $\mathbf{F}_{\text{tot}}$ enters also indirectly into Eq. (B.9) via $\mathbf{u}_{\text{macro}}$ which in the Guo forcing scheme is needed for the calculation of $\mathbf{f}^{\text{eq}}$. However, as $\mathbf{u}_{\text{macro}}$ itself is already scaled by $(1 - n_s)$ (cf. Eq. (7)), the factor $(1 - n_s)$ might be unintentionally considered several times for the force calculation.

Now, considering the Shan–Chen forcing scheme, the situation is much clearer. $\mathbf{F}_{\text{tot}}$ is only indirectly incorporated into $\mathbf{u}^{\text{eq}}$ (cf. Eq. (6)) which in the Shan–Chen forcing scheme is needed for the calculation of $\mathbf{f}^{\text{eq}}$. Thus, a repeated scaling by $(1 - n_s)$ is impossible.

Nevertheless, the actual reason why GS-WBS in Guo forcing leads to velocity discontinuities, while it does not when using the HMCSC in the Shan–Chen forcing scheme remains still unclear. A detailed analysis would be necessary which, however, goes far beyond the scope of this study.

Appendix C. Data

C.1. Maximum velocity in open boundary flow

The maximum velocities in lattice units for the open boundary flow validation test are presented in Table C.1.

C.2. Structure generation of homogenized separator

The homogenized separator structure has been created by downsampling the original binarized image by a factor of 20 in each direction. The original structure consisted of $600 \times 820 \times 560$ voxels with a voxel length of $2.19 \cdot 10^{-8}$ m. This structure has been subdivided into $20 \times 20 \times 20$ cubes, with the volume fraction of each cube being the mean volume fraction of its containing voxels. The resulting structure is of shape $30 \times 41 \times 28$. The voxel length, i.e. $4.38 \cdot 10^{-7}$ m, is identical to that of voxels of the electrode structure. But since the electrode structure is much larger, the separator has been stacked multiple times in both directions perpendicular to the filling direction to fit the dimensions of the electrode.

This procedure seems trivial and one could get the impression that it would be possible to run simulations using the gray values from CT images directly. However, as discussed in Ref. Baveye et al. (2017), this is not the case. The model parameter called the bounce-back fraction n_s does not correspond to the physical bounce-back fraction that is determined through images. With no information about the actual penetrability of the material, the relation between the physical parameter and the model parameter can only be guessed. To overcome this limitation, investigating a method for converting both will be one topic of our future research.

Appendix D. Supplementary data

Supplementary material related to this article can be found online at https://doi.org/10.1016/j.advwatres.2022.104320.

References

An, S., Zhan, Y., Yao, J., Yu, H.W., Niasar, V., 2020. A greyscale volumetric lattice Boltzmann method for upscaling pore-scale two-phase flow. Adv. Water Resour. 144, 103711. http://dx.doi.org/10.1016/j.advwatres.2020.103711.

Bai, B., Elgmati, M., Zhang, H., Wei, M., 2013. Rock characterization of fayetteville shale gas plays. Fuel 105, 645–652. http://dx.doi.org/10.1016/j.fuel.2012.09.043.

Baveye, P.C., Pot, V., Garnier, P., 2017. Accounting for sub-resolution pores in models of water and solute transport in soils based on computed tomography images: Are we there yet? J. Hydrol. 555, 253–256. http://dx.doi.org/10.1016/j.jhydrol.2017.10.021.

Bhatnagar, P.L., Gross, E.P., Krook, M., 1954. A model for collision processes in gases. I. Small amplitude processes in charged and neutral one-component systems. Phys. Rev. 94 (3), 511–525. http://dx.doi.org/10.1103/PhysRev.94.511.

Blunt, M.J., Bijeljic, B., Dong, H., Gharbi, O., Iglauer, S., Mostaghimi, P., Paluszny, A., Pentland, C., 2013. Pore-scale imaging and modelling. Adv. Water Resour. 51, 197–216. http://dx.doi.org/10.1016/j.advwatres.2012.03.003.

Chen, L., Kang, Q., Mu, Y., He, Y.L., Tao, W.Q., 2014. A critical review of the pseudopotential multiphase lattice Boltzmann model: Methods and applications. Int. J. Heat Mass Transfer 76, 210–236. http://dx.doi.org/10.1016/j.ijheatmasstransfer.2014.04.032.

Chen, Y., Zhu, K., 2008. A study of the upper limit of solid scatters density for gray lattice Boltzmann method. Acta Mech. Sinica 24 (5), 515–522. http://dx.doi.org/10.1007/s10409-008-0167-9.

Connington, K., Lee, T., 2012. A review of spurious currents in the lattice Boltzmann method for multiphase flows. J. Mech. Sci. Technol. 26 (12), 3857–3863. http://dx.doi.org/10.1007/s12206-012-1011-5.

Danner, T., Eswara, S., Schulz, V.P., Latz, A., 2016. Characterization of gas diffusion electrodes for metal-air batteries. J. Power Sources 324, 646–656. http://dx.doi.org/10.1016/j.jpowsour.2016.05.108.

Dardis, O., McCloskey, J., 1998. Lattice Boltzmann scheme with real numbered solid density for the simulation of flow in porous media. Phys. Rev. E 57 (4), 4834–4837. http://dx.doi.org/10.1103/PhysRevE.57.4834.

Das, S., Mitra, S.K., 2013. Different regimes in vertical capillary filling. Phys. Rev. E 87 (6), 063005. http://dx.doi.org/10.1103/PhysRevE.87.063005.

Das, S., Waghmare, P.R., Mitra, S.K., 2012. Early regimes of capillary filling. Phys. Rev. E 86 (6), 1–5. http://dx.doi.org/10.1103/PhysRevE.86.067301.

Dentz, M., Le Borgne, T., Englert, A., Bijeljic, B., 2011. Mixing, spreading and reaction in heterogeneous media: A brief review. J. Contam. Hydrol. 120–121 (C), 1–17. http://dx.doi.org/10.1016/j.jconhyd.2010.05.002.

Diewald, F., Lautenschlaeger, M.P., Stephan, S., Langenbach, K., Kuhn, C., Seckler, S., Bungartz, H.-J., Hasse, H., Müller, R., 2020. Molecular dynamics and phase field simulations of droplets on surfaces with wettability gradient. Comput. Methods Appl. Mech. Engrg. 361, 112773. http://dx.doi.org/10.1016/j.cma.2019.112773.

Freed, D.M., 1998. Lattice-Boltzmann method for macroscopic porous media modeling. Internat. J. Modern Phys. C 09 (08), 1491–1503. http://dx.doi.org/10.1142/S0129183198001357.

Gao, J., Xing, H., Tian, Z., Muhlhaus, H., 2014. Lattice Boltzmann modeling and evaluation of fluid flow in heterogeneous porous media involving multiple matrix constituents. Computers & Geosciences 62, 198–207. http://dx.doi.org/10.1016/j.cageo.2013.07.019.

Ghezzehei, T.A., 2012. Linking sub-pore scale heterogeneity of biological and geochemical deposits with changes in permeability. Adv. Water Resour. 39, 1–6. http://dx.doi.org/10.1016/j.advwatres.2011.12.015.

Ginzburg, I., 2008. Consistent lattice Boltzmann schemes for the Brinkman model of porous flow and infinite Chapman-Enskog expansion. Phys. Rev. E 77 (6), 066704. http://dx.doi.org/10.1103/PhysRevE.77.066704.

Ginzburg, I., 2016. Comment on "an improved gray lattice Boltzmann model for simulating fluid flow in multi-scale porous media": Intrinsic links between LBE Brinkman schemes. Adv. Water Resour. 88, 241–249. http://dx.doi.org/10.1016/j.advwatres.2014.05.007.

Ginzburg, I., Silva, G., Talon, L., 2015. Analysis and improvement of Brinkman lattice Boltzmann schemes: Bulk, boundary, interface. similarity and distinctness with finite elements in heterogeneous porous media. Phys. Rev. E 91 (2), 1–32. http://dx.doi.org/10.1103/PhysRevE.91.023307.

Gostick, J.T., Ioannidis, M.A., Fowler, M.W., Pritzker, M.D., 2008. Direct measurement of the capillary pressure characteristics of water-air-gas diffusion layer systems for PEM fuel cells. Electrochem. Commun. 10 (10), 1520–1523. http://dx.doi.org/10.1016/j.elecom.2008.08.008.

Guo, Z., Zhao, T.S., 2002. Lattice Boltzmann model for incompressible flows through porous media. Phys. Rev. E 66 (3), 036304. http://dx.doi.org/10.1103/PhysRevE.66.036304.

Guo, Z., Zheng, C., Shi, B., 2002. Discrete lattice effects on the forcing term in the lattice Boltzmann method. Phys. Rev. E 65 (4), 046308. http://dx.doi.org/10.1103/PhysRevE.65.046308.

Hassannayebi, N., Jammernegg, B., Schritter, J., Arnold, P., Enzmann, F., Kersten, M., Loibner, A.P., Fernø, M., Ott, H., 2021. Relationship between microbial growth and hydraulic properties at the sub-pore scale. Transp. Porous Media 139 (3), 579–593. http://dx.doi.org/10.1007/s11242-021-01680-5.

Huang, H., Thorne, D.T., Schaap, M.G., Sukop, M.C., 2007. Proposed approximation for contact angles in Shan-and-Chen-type multicomponent multiphase lattice Boltzmann models. Phys. Rev. E 76 (6), 1–6. http://dx.doi.org/10.1103/PhysRevE.76.066701.

Jung, H., Meile, C., 2021. Pore-scale numerical investigation of evolving porosity and permeability driven by biofilm growth. Transp. Porous Media 139 (2), 203–221. http://dx.doi.org/10.1007/s11242-021-01654-7.

Kang, Q., Lichtner, P.C., Zhang, D., 2007. An improved lattice Boltzmann model for multicomponent reactive transport in porous media at the pore scale. Water Resour. Res. 43 (12), 1–12. http://dx.doi.org/10.1029/2006WR005551.

Kang, D.H., Yang, E., Yun, T.S., 2019. Stokes-Brinkman flow simulation based on 3-D μ-CT images of porous rock using grayscale pore voxel permeability. Water Resour. Res. 55 (5), 4448–4464. http://dx.doi.org/10.1029/2018WR024179.

Kang, Q., Zhang, D., Chen, S., 2002a. Displacement of a two-dimensional immiscible droplet in a channel. Phys. Fluids 14 (9), 3203–3214. http://dx.doi.org/10.1063/1.1499125.

Kang, Q., Zhang, D., Chen, S., 2002b. Unified lattice Boltzmann method for flow in multiscale porous media. Phys. Rev. E 66 (5), 056307. http://dx.doi.org/10.1103/PhysRevE.66.056307.

Kang, Q., Zhang, D., Chen, S., 2004. Immiscible displacement in a channel: simulations of fingering in two dimensions. Adv. Water Resour. 27 (1), 13–22. http://dx.doi.org/10.1016/j.advwatres.2003.10.002.

Karpyn, Z., Halleck, P., Grader, A., 2009. An experimental study of spontaneous imbibition in fractured sandstone with contrasting sedimentary layers. J. Pet. Sci. Eng. 67 (1–2), 48–56. http://dx.doi.org/10.1016/j.petrol.2009.02.014.

Krevor, S.C.M., Pini, R., Zuo, L., Benson, S.M., 2012. Relative permeability and trapping of CO_2 and water in sandstone rocks at reservoir conditions. Water Resour. Res. 48 (2), 1–16. http://dx.doi.org/10.1029/2011WR010859.

Krueger, T., Kusumaatmaja, H., Kuzmin, A., Shardt, O., Silva, G., Viggen, E., 2016. The Lattice Boltzmann Method: Principles and Practice. Springer.

Latt, J., Malaspinas, O., Kontaxakis, D., Parmigiani, A., Lagrava, D., Brogi, F., Belgacem, M.B., Thorimbert, Y., Leclaire, S., Li, S., Marson, F., Lemus, J., Kotsalos, C., Conradin, R., Coreixas, C., Petkantchin, R., Raynaud, F., Beny, J., Chopard, B., 2021. Palabos: parallel lattice Boltzmann solver. Comput. Math. Appl. 81, 334–350. http://dx.doi.org/10.1016/j.camwa.2020.03.022.

Laubach, S.E., Lander, R.H., Criscenti, L.J., Anovitz, L.M., Urai, J.L., Pollyea, R.M., Hooker, J.N., Narr, W., Evans, M.A., Kerisit, S.N., Olson, J.E., Dewers, T., Fisher, D., Bodnar, R., Evans, B., Dove, P., Bonnell, L.M., Marder, M.P., Pyrak-Nolte, L., 2019. The role of chemistry in fracture pattern development and opportunities to advance interpretations of geological materials. Rev. Geophys. 57 (3), 1065–1111. http://dx.doi.org/10.1029/2019RG000671.

Lautenschlaeger, M.P., Hasse, H., 2019a. Shear-rate dependence of thermodynamic properties of the Lennard-Jones truncated and shifted fluid by molecular dynamics simulations. Phys. Fluids 31 (6), 063103. http://dx.doi.org/10.1063/1.5090489.

Lautenschlaeger, M.P., Hasse, H., 2019b. Transport properties of the Lennard-Jones truncated and shifted fluid from non-equilibrium molecular dynamics simulations. Fluid Phase Equilib. 482, 38–47. http://dx.doi.org/10.1016/j.fluid.2018.10.019.

Lautenschlaeger, M.P., Hasse, H., 2020. Thermal, caloric and transport properties of the Lennard–Jones truncated and shifted fluid in the adsorbed layers at dispersive solid walls. Mol. Phys. 118 (9–10), e1669838. http://dx.doi.org/10.1080/00268976.2019.1669838.

Lautenschlaeger, M.P., Prifling, B., Kellers, B., Weinmiller, J., Danner, T., Schmidt, V., Latz, A., 2022. Understanding electrolyte filling of lithium-ion battery electrodes on the pore scale using the lattice Boltzmann method. Batter. Supercaps 7 (5), e202200090. http://dx.doi.org/10.1002/batt.202200090.

Lei, S., Shi, Y., 2019. Separate-phase model and its lattice Boltzmann algorithm for liquid-vapor two-phase flows in porous media. Phys. Rev. E 99 (5), 053302. http://dx.doi.org/10.1103/PhysRevE.99.053302.

Li, R., Yang, Y.S., Pan, J., Pereira, G.G., Taylor, J.A., Clennell, B., Zou, C., 2014. Lattice Boltzmann modeling of permeability in porous materials with partially percolating voxels. Phys. Rev. E 90 (3), 033301. http://dx.doi.org/10.1103/PhysRevE.90.033301.

Li, K., Zhang, D., Bian, H., Meng, C., Yang, Y., 2015. Criteria for applying the Lucas-Washburn law. Sci. Rep. 5 (1), 14085. http://dx.doi.org/10.1038/srep14085.

Liu, H., Kang, Q., Leonardi, C.R., Schmieschek, S., Narváez, A., Jones, B.D., Williams, J.R., Valocchi, A.J., Harting, J., 2016. Multiphase lattice Boltzmann simulations for porous media applications: A review. Comput. Geosci. 20 (4), 777–805. http://dx.doi.org/10.1007/s10596-015-9542-3.

McDonald, P.J., Turner, M.N., 2016. Combining effective media and multi-phase methods of lattice Boltzmann modelling for the characterisation of liquid-vapour dynamics in multi-length scale heterogeneous structural materials. Modelling Simulation Mater. Sci. Eng. 24 (1), 015010. http://dx.doi.org/10.1088/0965-0393/24/1/015010.

Mehmani, A., Mehmani, Y., Prodanović, M., Balhoff, M., 2015. A forward analysis on the applicability of tracer breakthrough profiles in revealing the pore structure of tight gas sandstone and carbonate rocks. Water Resour. Res. 51 (6), 4751–4767. http://dx.doi.org/10.1002/2015WR016948.

Mehmani, Y., Tchelepi, H.A., 2018. Multiscale computation of pore-scale fluid dynamics: Single-phase flow. J. Comput. Phys. 375, 1469–1487. http://dx.doi.org/10.1016/j.jcp.2018.08.045.

Mehmani, A., Verma, R., Prodanović, M., 2020. Pore-scale modeling of carbonates. Mar. Pet. Geol. 114, 104141. http://dx.doi.org/10.1016/j.marpetgeo.2019.104141.

Mu, L., Liao, X., Chen, Z., Zou, J., Chu, H., Li, R., 2019. Analytical solution of Buckley-Leverett equation for gas flooding including the effect of miscibility with constant-pressure boundary. Energy Explor. Exploit. 37 (3), 960–991. http://dx.doi.org/10.1177/0144598719842335.

Ning, Y., Wei, C., Qin, G., 2019. A unified grayscale lattice Boltzmann model for multiphase fluid flow in vuggy carbonates. Adv. Water Resour. 124, 68–83. http://dx.doi.org/10.1016/j.advwatres.2018.12.007.

Parnas, R.S., Howard, J.G., Luce, T.L., Advani, S.G., 1995. Permeability characterization. Part 1: A proposed standard reference fabric for permeability. Polym. Compos. 16 (6), 429–445. http://dx.doi.org/10.1002/pc.750160602.

Pereira, G.G., 2016. Grayscale lattice Boltzmann model for multiphase heterogeneous flow through porous media. Phys. Rev. E 93 (6), 1–14. http://dx.doi.org/10.1103/PhysRevE.93.063301.

Pereira, G.G., 2019. Fluid flow, relative permeabilities and capillary pressure curves through heterogeneous porous media. Appl. Math. Model. 75, 481–493. http://dx.doi.org/10.1016/j.apm.2019.05.050.

Phelan, F.R., Wise, G., 1996. Analysis of transverse flow in aligned fibrous porous media. Composites A 27 (1), 25–34. http://dx.doi.org/10.1016/1359-835X(95)00016-U.

Pini, R., Krevor, S.C., Benson, S.M., 2012. Capillary pressure and heterogeneity for the CO_2/water system in sandstone rocks at reservoir conditions. Adv. Water Resour. 38, 48–59. http://dx.doi.org/10.1016/j.advwatres.2011.12.007.

Sauter, C., Zahn, R., Wood, V., 2020. Understanding electrolyte infilling of lithium ion batteries. J. Electrochem. Soc. 167 (10), 100546. http://dx.doi.org/10.1149/1945-7111/ab9bfd.

Sbragaglia, M., Benzi, R., Biferale, L., Succi, S., Sugiyama, K., Toschi, F., 2007. Generalized lattice Boltzmann method with multirange pseudopotential. Phys. Rev. E 75 (2), 026702. http://dx.doi.org/10.1103/PhysRevE.75.026702.

Shan, X., 2006. Analysis and reduction of the spurious current in a class of multiphase lattice Boltzmann models. Phys. Rev. E 73 (4), 047701. http://dx.doi.org/10.1103/PhysRevE.73.047701.

Shan, X., Chen, H., 1993. Lattice Boltzmann model for simulating flows with multiple phases and components. Phys. Rev. E 47 (3), 1815–1819. http://dx.doi.org/10.1103/PhysRevE.47.1815.

Shodiev, A., Primo, E., Arcelus, O., Chouchane, M., Osenberg, M., Hilger, A., Manke, I., Li, J., Franco, A.A., 2021. Insight on electrolyte infiltration of lithium ion battery electrodes by means of a new three-dimensional-resolved lattice Boltzmann model. Energy Storage Mater. 38, 80–92. http://dx.doi.org/10.1016/j.ensm.2021.02.029.

Silva, G., Ginzburg, I., 2015. The permeability and quality of velocity field in a square array of solid and permeable cylindrical obstacles with the TRT–LBM and FEM Brinkman schemes. C. R. Méc. 343 (10–11), 545–558. http://dx.doi.org/10.1016/j.crme.2015.05.003.

Sok, R.M., Varslot, T., Ghous, A., Latham, S., Sheppard, A.P., Knackstedt, M.A., 2010. Pore scale characterization of carbonates at multiple scales: Integration of micro-CT, BSEM, and FIBSEM. Petrophysics 51 (6), 379–387.

Soulaine, C., Creux, P., Tchelepi, H.A., 2019. Micro-continuum framework for pore-scale multiphase fluid transport in shale formations. Transp. Porous Media 127 (1), 85–112. http://dx.doi.org/10.1007/s11242-018-1181-4.

Spaid, M.A.A., Phelan, F.R., 1997. Lattice Boltzmann methods for modeling microscale flow in fibrous porous media. Phys. Fluids 9 (9), 2468–2474. http://dx.doi.org/10.1063/1.869392.

Spaid, M.A., Phelan, F.R., 1998. Modeling void formation dynamics in fibrous porous media with the lattice Boltzmann method. Composites A 29 (7), 749–755. http://dx.doi.org/10.1016/S1359-835X(98)00031-1.

Steefel, C., DePaolo, D., Lichtner, P., 2005. Reactive transport modeling: An essential tool and a new research approach for the Earth sciences. Earth and Planet. Sci. Lett. 240 (3–4), 539–558. http://dx.doi.org/10.1016/j.epsl.2005.09.017.

Tavangarrad, A.H., Hassanizadeh, S.M., Rosati, R., Digirolamo, L., van Genuchten, M.T., 2019. Capillary pressure–saturation curves of thin hydrophilic fibrous layers: effects of overburden pressure, number of layers, and multiple imbibition–drainage cycles. Text. Res. J. 89 (23–24), 4906–4915. http://dx.doi.org/10.1177/0040517519844209.

Thorne, D., Sukop, M., 2004. Lattice Boltzmann model for the elder problem. In: Miller, C.T., Pinder, G.F. (Eds.), Computational Methods in Water Resources, Vol. 2. In: Developments in Water Science, vol. 55, Elsevier, pp. 1549–1557. http://dx.doi.org/10.1016/S0167-5648(04)80165-5.

Walsh, S.D., Burwinkle, H., Saar, M.O., 2009. A new partial-bounceback lattice Boltzmann method for fluid flow through heterogeneous media. Comput. Geosci. 35 (6), 1186–1193. http://dx.doi.org/10.1016/j.cageo.2008.05.004.

Washburn, E.W., 1921. The dynamics of capillary flow. Phys. Rev. 17 (3), 273–283. http://dx.doi.org/10.1103/PhysRev.17.273.

Welge, H.J., 1952. A simplified method for computing oil recovery by gas or water drive. J. Pet. Technol. 4 (04), 91–98. http://dx.doi.org/10.2118/124-G.

Westhoff, D., Manke, I., Schmidt, V., 2018. Generation of virtual lithium-ion battery electrode microstructures based on spatial stochastic modeling. Comput. Mater. Sci. 151, 53–64. http://dx.doi.org/10.1016/j.commatsci.2018.04.060.

Weydanz, W., Reisenweber, H., Gottschalk, A., Schulz, M., Knoche, T., Reinhart, G., Masuch, M., Franke, J., Gilles, R., 2018. Visualization of electrolyte filling process and influence of vacuum during filling for hard case prismatic lithium ion cells by neutron imaging to optimize the production process. J. Power Sources 380, 126–134. http://dx.doi.org/10.1016/j.jpowsour.2018.01.081.

Wood, D.L., Li, J., Daniel, C., 2015. Prospects for reducing the processing cost of lithium ion batteries. J. Power Sources 275, 234–242. http://dx.doi.org/10.1016/j.jpowsour.2014.11.019.

Yehya, A., Naji, H., Sukop, M.C., 2015. Simulating flows in multi-layered and spatially-variable permeability media via a new gray lattice Boltzmann model. Comput. Geotech. 70, 150–158. http://dx.doi.org/10.1016/j.compgeo.2015.07.017.

Yoshida, H., Hayashi, H., 2014. Transmission-reflection coefficient in the lattice Boltzmann method. J. Stat. Phys. 155 (2), 277–299. http://dx.doi.org/10.1007/s10955-014-0953-7.

Yu, Z., Fan, L.-S., 2010. Multirelaxation-time interaction-potential-based lattice Boltzmann model for two-phase flow. Phys. Rev. E 82 (4), 046708. http://dx.doi.org/10.1103/PhysRevE.82.046708.

Yuan, G., Cao, Y., Schulz, H.-M., Hao, F., Gluyas, J., Liu, K., Yang, T., Wang, Y., Xi, K., Li, F., 2019. A review of feldspar alteration and its geological significance in sedimentary basins: From shallow aquifers to deep hydrocarbon reservoirs. Earth-Sci. Rev. 191 (October 2017), 114–140. http://dx.doi.org/10.1016/j.earscirev.2019.02.004.

Zalzale, M., Ramaioli, M., Scrivener, K.L., McDonald, P.J., 2016. Gray free-energy multiphase lattice Boltzmann model with effective transport and wetting properties. Phys. Rev. E 94 (5), 1–13. http://dx.doi.org/10.1103/PhysRevE.94.053301.

Zhang, X., Crawford, J.W., Flavel, R.J., Young, I.M., 2016. A multi-scale lattice Boltzmann model for simulating solute transport in 3D X-ray micro-tomography images of aggregated porous materials. J. Hydrol. 541, 1020–1029. http://dx.doi.org/10.1016/j.jhydrol.2016.08.013.

Zhang, Q., Yu, H., Li, X., Liu, T., Hu, J., 2020. A new upscaling method for fluid flow simulation in highly heterogeneous unconventional reservoirs. Geofluids 2020, 1–11. http://dx.doi.org/10.1155/2020/6213183.

Zhao, H., Ning, Z., Wang, Q., Zhang, R., Zhao, T., Niu, T., Zeng, Y., 2015. Petrophysical characterization of tight oil reservoirs using pressure-controlled porosimetry combined with rate-controlled porosimetry. Fuel 154, 233–242. http://dx.doi.org/10.1016/j.fuel.2015.03.085.

Zhu, J., Ma, J., 2013. An improved gray lattice Boltzmann model for simulating fluid flow in multi-scale porous media. Adv. Water Resour. 56, 61–76. http://dx.doi.org/10.1016/j.advwatres.2013.03.001.

Zhu, J., Ma, J., 2018. Extending a gray lattice Boltzmann model for simulating fluid flow in multi-scale porous media. Sci. Rep. 8 (1), 1–19. http://dx.doi.org/10.1038/s41598-018-24151-2.

Zhu, L., Zhang, H., Xiao, L., Bazylak, A., Gao, X., Sui, P.-C., 2021. Pore-scale modeling of gas diffusion layers: Effects of compression on transport properties. J. Power Sources 496 (June 2020), 229822. http://dx.doi.org/10.1016/j.jpowsour.2021.229822.